Voltage-Biased Superconducting Bolometers for Infrared and mm-Waves

by

Jan Mathias Gildemeister

Diplom-Physiker (Universität Heidelberg) 1995

A dissertation submitted in partial satisfaction

of the requirements for the degree of

Doctor of Philosophy

in

Physics

in the

GRADUATE DIVISION

of the

UNIVERSITY OF CALIFORNIA, BERKELEY

Committee in charge:

Professor Paul L. Richards, Chair

Professor John Clarke

Professor Theodore VanDuzer

Fall 2000

The dissertation of Jan Mathias Gildemeister is approved:

Paul L. Richards, Chair — Date

John Clarke — Date

Theodore VanDuzer — Date

University of California, Berkeley

Fall 2000

Voltage-Biased Superconducting Bolometers for Infrared and mm-Waves

Abstract

Voltage-Biased Superconducting Bolometers for Infrared and mm-Waves

by

Jan Mathias Gildemeister

Doctor of Philosophy in Physics

University of California, Berkeley

Professor Paul L. Richards, Chair

We describe the design, fabrication, and testing of superconducting bolometers for far-infrared and millimeter waves. The bolometers are voltage biased and the current is read out with a commercial SQUID amplifier. Electrothermal feedback makes the devices null-detectors with reduced response time and enhanced linearity.

Three types of voltage biased superconducting bolometers are discussed. The first two types are operated at a base temperature of $T_0 = 264$mK and are intended for use in astrophysics experiments such as measurements of

the anisotropy in the temperature and polarization of the cosmic microwave background. Bolometers fabricated in a mesh structure resembling a spider-web are designed for use in horn-coupled arrays. Bolometers made with a square mesh structure can be assembled into close-packed arrays to fill the focal plane of a telescope. The third type is designed for use in a far-infrared Fourier spectrometer. It is suspended by a membrane and is operated at the temperature of liquid He, $T_0 = 4.2$K.

The important operational parameters of all devices are discussed. Measurements of time constants and noise spectra are presented. The first two types show a wide feature of noise not explained by the basic theory. An alternative noise model is discussed in which additional noise arises from the combination of electrothermal feedback and a complex thermal circuit. This model explains the observed excess noise and is supported by data from other devices which were built specifically to test the model. The model shows that noise performance can be improved to fundamental limits by using low heat capacity metals for the bolometer components.

All devices are manufactured by standard microlithographic techniques. The design and fabrication process is described in detail and possible improvements are discussed.

Dedicated to my parents

Acknowledgements

This work would not have been possible without the love and endless support from my parents. I thank them for encouraging me to pursue my goals and for giving me great freedom in doing so. Only recently have I begun to understand how much this really means.

I thank Prof. Paul L. Richards for the privilege of working under his supervision. With his unusual dedication to training and teaching he has contributed greatly to the excellent education I have received at Berkeley. With his fairness and integrity he has set a lasting example for me. I thank Prof. Adrian T. Lee for teaching me many of my experimental skills, for being a great mentor and coworker, and, most of all, for being a reliable friend at all times. I am also indebted to Warren A. Holmes who shared his wisdom about silicon nitride and held my hand during my first steps in cryogenics.

Finally, I thank Dana Carr for being my best friend and an outstanding companion, for greatly supporting me in this work, and for putting up with the odd work hours of an experimental physicist.

Contents

List of Figures

Preface

Some of the work described in this dissertation has previously been published in refereed journals. Sections 3.2 and 3.3 are derived from references [1] and [2], respectively. Chapter 4 is closely related to reference [3].

Chapter 1

Introduction

The subject of this dissertation is the development, fabrication, and testing of very sensitive detectors for electromagnetic waves with wavelengths between a few hundred μm and several mm.

1.1 Scientific Applications

At this time, the strongest drivers for the development and improvement of detectors for the far-infrared and millimeter-waves (far-IR and MMW) are scientific applications in cosmology and astrophysics.

It is now generally agreed among astronomers and physicists that the universe began about 15 billion years ago in a cataclysmic event called the

Big Bang. In 1965 Penzias and Wilson discovered electromagnetic radiation which appeared to emanate uniformly from all directions in the sky [4]. This radiation is the cosmic microwave background (CMB) which is a remnant of the Big Bang. It originated about 300,000 years after the Big Bang when the universe had cooled sufficiently to allow protons and electrons to form neutral H atoms. At this point light could travel for the first time without being continuously scattered by ions and the universe became transparent. The CMB we see today is hence an image of the universe at this time of last scattering. Since then the expansion of the universe has shifted the CMB radiation to longer and longer wavelengths. Today the CMB displays the spectrum of a black body with a temperature of 2.7K. The maximum of this spectrum lies at a wavelength of $\approx$ 2mm. Most of the electromagnetic energy of the universe is contained in the CMB.

In 1990 the Cosmic Background Explorer (COBE) satellite showed that the CMB is not completely isotropic [5] but rather that the black body temperature measured at different points in the sky varies by $\approx 130\mu$K (rms). This temperature anisotropy contains information about the very beginning of the universe as well as about the parameters which govern its evolution. Several ground and balloon based experiments have begun to mine this in-

formation [6, 7] with increasing spatial resolution and sensitivity and further satellite missions are planned for the future [8]. Information about the angular power spectrum of the thermal fluctuations as well as about their statistics can be obtained by mapping the temperature anisotropy over a part of the sky. At small angular scales ($< 5^\circ$) this information puts constraints on important cosmological parameters such as the Hubble constant, the total density parameter, the cosmological constant, and the baryon content of the universe. At large angular scales ($> 5^\circ$) the temperature anisotropy should depend primarily on density fluctuations on large scales at the time of last scattering, providing an important test of the theory of inflation. This theory states that during a period of its early evolution the universe expanded exponentially, explaining correlations between parts of the sky which could otherwise not have been causally connected. Today the temperature anisotropy data are the most important tool to discriminate between different cosmological models.

The next step in the exploration of the CMB will be the detection and characterization of its polarization anisotropy. Polarization is expected to arise from Thomson scattering of CMB photons from electrons in the plasma which filled the universe before it became transparent. Measurements of

its anisotropy will test the theory of inflation and will provide an important check of the temperature anisotropy data. They will also make it possible to separate two components of the temperature anisotropy arising from density fluctuations and peculiar velocities at the surface of last scattering, respectively. Finally, they will provide information about star formation, improve the determination of cosmological parameters, and probe primordial magnetic fields.

Another important source of information arises from the Sunyaev Zel'dovic (SZ) effect which is the Compton-scattering of CMB photons with hot gas in clusters of galaxies. This process creates a well-defined distortion of the black body spectrum which can be separated cleanly from the temperature anisotropy. Measurements of the SZ-effect will contribute greatly to our understanding of the formation of structure and of galaxies, allow the determination of the Hubble constant and large-scale peculiar velocity fields (i.e. deviations from the Hubble flow), and facilitate the detection of clusters of galaxies at high red-shifts.

In addition to CMB science, interesting science goals in the far-IR and MMW regime include the detection of new extragalactic sources and the measurement of the spectra of star burst galaxies, active galactic nuclei,

radio galaxies, and quasars.

Improvements in the sensitivity of detectors in recent years have enabled precise new measurements of the CMB temperature anisotropy. As discussed, however, there is a wealth of additional information still to be found in the far-IR and MMW range. To extract this information, significant further improvements in the sensitivity of experiments are required. For example, the CMB polarization anisotropy is predicted to be an order of magnitude smaller in ΔT than the temperature anisotropy. A possible curl component of the polarization anisotropy, which would be a signature of gravity waves produced during inflation, is estimated to be yet at least another order of magnitude smaller.

Outside of astrophysics and cosmology, far-IR detectors are used for spectroscopy with a Fourier transform spectrometer. Transmittance measurements are made by switching the sample into and out of the light path. In addition, the absolute level of the signal is obtained by measuring the peak in the interferogram at zero path difference. Both procedures can change the background loading on the detector dramatically and therefore demand detectors with linear response over a wide operating range. The need to avoid low-frequency noise and 60Hz interference in continuously scanned in-

terferometers makes it desirable to operate at fringe frequencies above 60Hz, demanding detectors with a high response frequency. Existing detectors offer only moderate performance in linearity and speed and an improvement in detector technology could greatly increase the precision and convenience of spectroscopic measurements.

1.2 Competing Receiver Technologies

Receivers for electromagnetic radiation act as transducers which receive photons and produce an electrical signal which can be amplified and recorded. Receivers typically consist of components which can be divided into three functional categories:

- Amplifiers
- Mixers, which multiply two incoming signals of different frequencies and produce an output signal at their difference frequency
- Detectors, which typically convert incoming power into a DC output signal

Photon receivers are used for narrow band applications such as spectroscopy and for broad band applications such as photometry. The three

types of receivers used predominantly for broad band applications are:

- Coherent receivers with or without mixers
- Thermal direct detectors
- Photon direct detectors

Coherent receivers respond to the electric field strength of the incoming signal and can therefore preserve information about the phase of incoming photons. Some of these receivers operate by mixing the electric fields of the incoming photon and of a coherent local oscillator in a mixer which is a fast square law device. The signal at the beat frequency is then amplified and detected. Depending on the wavelength of interest, thermonic diodes, tunnel diodes, and thermal or photon mixers are used. Other receivers amplify the incoming signal before it is mixed with the field of the local oscillator and/or detected. For best performance high electron mobility transistors (HEMTs) are commonly used as amplifiers. While coherent receivers monopolize applications at radio-frequencies, their spectral bandwidth is inherently narrow and they are rarely used for broad band applications at wavelengths below 3mm.

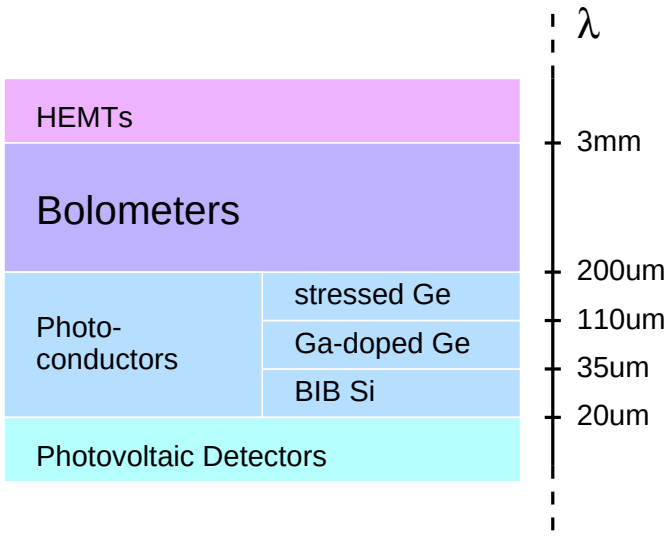

Figure 1.1: An overview of different broad band receiver technologies and the range of wavelengths in which they are predominantly used.

At shorter wavelengths thermal devices and photon devices together with an output amplifier are most widely used as mixers or direct detectors. The distinguishing characteristic between the two types is not that one can necessarily detect an individual photon. It is rather that in a thermal device the excitation generated by an incoming photon relaxes to a thermal distribution before it is detected, while in a photon device the excitation is detected before it relaxes.

Photon devices used in the infrared are typically either photovoltaic devices (photodiodes) or extrinsic photoconductors [9]. In photodiodes a photon creates charge carriers in a depleted zone between oppositely doped layers of a semiconductor. The response of photodiodes is limited to wavelengths below 20μm by the bandgaps of the available high quality intrinsic semiconductors. In extrinsic photoconductors a photon excites electrons (holes) from the impurity band to the conduction (valence) band of a doped semiconductor resulting in a change of conductivity. Detectors made from doped Si or Ge can be used for wavelengths up to 110μm. In Ge:Ga the excitation energy can be shifted by applying uniaxial stress, extending the cut-off to $\approx 200\mu$m. For all photon detectors the operating temperature must be low enough that the number of thermally generated carriers is much smaller than the number

of those generated by incoming photons, i.e. $k_B T \ll hc/\lambda_c$, where λ_c is the cut-off wavelength. This means that photon direct detectors for the range of wavelengths considered here must be operated at temperatures well below 77K, sometimes below 4.2K.

Thermal devices used in the infrared are typically bolometers, which can be used as mixers or as direct detectors. This dissertation deals with bolometric direct detectors which are the most sensitive broadband detectors for wavelengths from 200μm to 3mm. While photovoltaic detectors and extrinsic Si detectors have greatly benefitted from research undertaken for military applications and are available today in arrays with millions of pixels, bolometers are little developed in comparison. Bolometer performance is now beginning to approach fundamental noise limits and the largest arrays available consist of $\approx$ 100 bolometers. The goal is to develop devices which operate at fundamental noise limits over a wide range of response frequencies and which can be made and read out in large arrays with 10^3 - 10^4 elements. The work reported in this dissertation is a contribution towards this goal.

Chapter 2

Bolometer Theory

2.1 Thermal Radiation Detectors

Thermal radiation detectors in their most simple form consist of an absorbing element of heat capacity C which is connected to a heat sink by a weak thermal link. If a power P is absorbed in C, the detector temperature T rises above the temperature of the heat sink T_0.

The average thermal conductance $\bar{G}$ of the weak thermal link is defined by

$$P = \bar{G} \cdot (T - T_0), \tag{2.1}$$

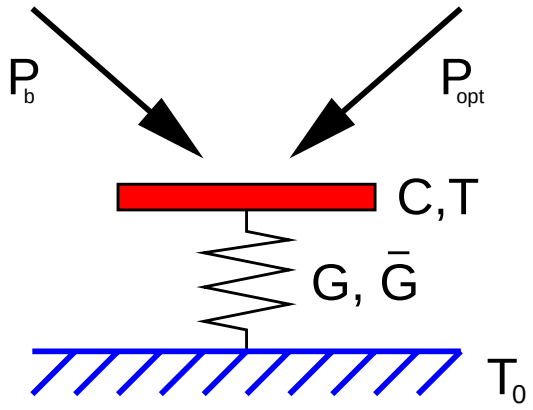

Figure 2.1: Lumped element thermal model of a thermal radiation detector.

and its dynamic thermal conductance G is given by

$$G = \frac{dP}{dT}. \tag{2.2}$$

If the power absorbed in the detector changes instantaneously to a new value P', T changes as a function of time, approaching its new value $T' = T_0 + P'/\bar{G}$ with a thermal time constant

$$\tau = \frac{C}{G}. \tag{2.3}$$

Thermal radiation detectors detect changes in P by measuring changes in T. Examples of thermal radiation detectors are the pyroelectric detector, the Golay pneumatic detector, and the bolometer.

The bolometer was invented by Langley [10]. It uses an electrical resistance thermometer (thermistor) to measure changes in T. A sensitive bolometer employs a thermometer material which shows a strong temperature-dependence of its resistivity around the operating temperature T. Doped semiconductors such as neutron-transmutation-doped (NTD) Ge crystals [11] or ion-implanted Si are commonly used for IR-bolometers.

2.2 Electrothermal feedback

The thermistor is biased electrically and a bias power is dissipated in it. The total power absorbed in the bolometer is the sum of the incident optical power and the bias power.

$$P = P_{opt} + P_b. \tag{2.4}$$

The fact that P_b varies with resistance and therefore with temperature introduces an electrothermal feedback into the system. If P_b increases with T this is a positive feedback, if P_b decreases the feedback is negative.

The thermistor materials employed by non-superconducting bolometers typically show a decrease of resistivity with temperature, i.e. $dR/dT < 0$ where R is the resistance of the thermistor. Typically, such a bolometer is operated with a constant current bias I_b and the voltage $V = RI_b$ across the detector is measured. The bias power is then $P_b = {I_b}^2 R$ so

$$\frac{dP_b}{dR} = {I_b}^2 > 0 \quad \Longrightarrow \quad \frac{dP_b}{dT} < 0, \tag{2.5}$$

and the electrothermal feedback is negative. In bolometers employing NTD sensors only moderate values of dR/dT are achieved and the feedback is relatively weak.

2.3 The Voltage-Biased Superconducting Bolometer

As discussed, the resistivity of the thermistor material has to show a strong dependence on temperature at the operating-temperature of the bolometer. The strongest known dependence of resistivity on temperature occurs in the resistive transition of a superconductor. A superconductor with a suitable critical temperature T_c therefore appears as a natural choice for a thermistor material. Superconducting bolometers biased with a constant current have been built since 1943.

In this dissertation we will consider the case of a superconducting bolometer, biased in the resistive transition with a constant voltage V_b. Changes in the optical signal power lead to changes in the bias current I, which are measured. The bias power is

$$P_b = \frac{{V_b}^2}{R}. \tag{2.6}$$

Since $dR/dT > 0$ the feedback is negative

$$\frac{dP_b}{dT} = -\frac{{V_b}^2}{R^2}\frac{dR}{dT} < 0. \tag{2.7}$$

We now consider the case in which a small time-varying optical signal

$\delta P_{opt} \exp(i\omega t)$ is absorbed in the bolometer in addition to the constant power $P = P_b + P_{opt}$. This signal leads to a change in temperature $\delta T \exp(i\omega t)$ which in turn causes a change in the bias power, partially compensating for the change in optical power. Conservation of energy requires that

$$P + \delta P_{opt} e^{i\omega t} - \frac{{V_b}^2}{R^2}\frac{dR}{dT}\delta T e^{i\omega t} = \bar{G}(T - T_0) + (G + i\omega C)\delta T e^{i\omega t}. \tag{2.8}$$

The time-dependent part of equation 2.8 is

$$\delta P_{opt} = \left(\frac{P_b}{T}\alpha + G + i\omega C\right)\delta T, \tag{2.9}$$

where $\alpha = d(\log R)/d(\log T)$ is a dimensionless parameter quantifying the sharpness of the resistive transition at the bias point. The first term on the right side is due to the electrothermal feedback effect. We can define an effective complex thermal conductance which includes the effect of electrothermal feedback.

$$G_{eff} = \frac{P_b}{T}\alpha + G + i\omega C. \tag{2.10}$$

In analogy to electronic feedback circuits, we define a loop gain

$$\mathcal{L}(\omega) = -\frac{\delta P_b}{\delta P}. \tag{2.11}$$

It is a measure of the strength of the electrothermal feedback and from

equation 2.9 we see that

$$\mathcal{L}(\omega) = \frac{P_b \alpha}{GT(1 + i\omega\tau_0)} = \frac{\mathcal{L}}{1 + i\omega\tau_0}, \tag{2.12}$$

where $\mathcal{L}$ is the dc gain. The gain rolls off at $\omega = 1/\tau_0 = G/C$.

In a voltage-biased bolometer, the output signal is a change in the bias current. The current responsivity $S_I = dI/dP_{opt}$ is the change in output signal per unit change in incoming optical signal. From equation (2.9),

$$S_I = -\frac{1}{V_b} \frac{\mathcal{L}}{\mathcal{L} + 1} \frac{1}{1 + i\omega\tau}, \tag{2.13}$$

where

$$\tau = -\frac{\tau_0}{\mathcal{L} + 1} \tag{2.14}$$

is the effective time constant. Unlike the loop gain, the responsivity rolls off at the higher frequency $\omega = 1/\tau$. The electrothermal feedback speeds up the bolometer by a factor of $\mathcal{L} + 1$. In the limit of strong electrothermal feedback $\mathcal{L} \gg 1$, the current responsivity for frequencies $\omega \ll 1/\tau$ is simply determined by the bias voltage:

$$S_I = -\frac{1}{V_b} \tag{2.15}$$

This responsivity is independent of the power loading P_{opt}, which makes

the detector highly linear. It is also independent of the base temperature T_0 which isolates the detector from temperature fluctuations and drifts.

While electrothermal feedback occurs in all bolometers, the condition $\mathcal{L} \gg 1$ is only met in superconducting bolometers, because of the high value of α in the resistive transition. Linearity and reduced time constant are therefore key properties of the voltage-biased superconducting bolometer which distinguish it from conventional bolometers.

High values of $\mathcal{L}$ are in principle also a characteristic of current-biased superconducting bolometers. However, here the electrothermal feedback is positive and the device is inherently unstable if $\mathcal{L} \geq 1$. Current-biased devices could therefore only be operated with an external feedback system which artificially reduced the loop gain. This caused a variety of problems which did not let this type of detector be successful.

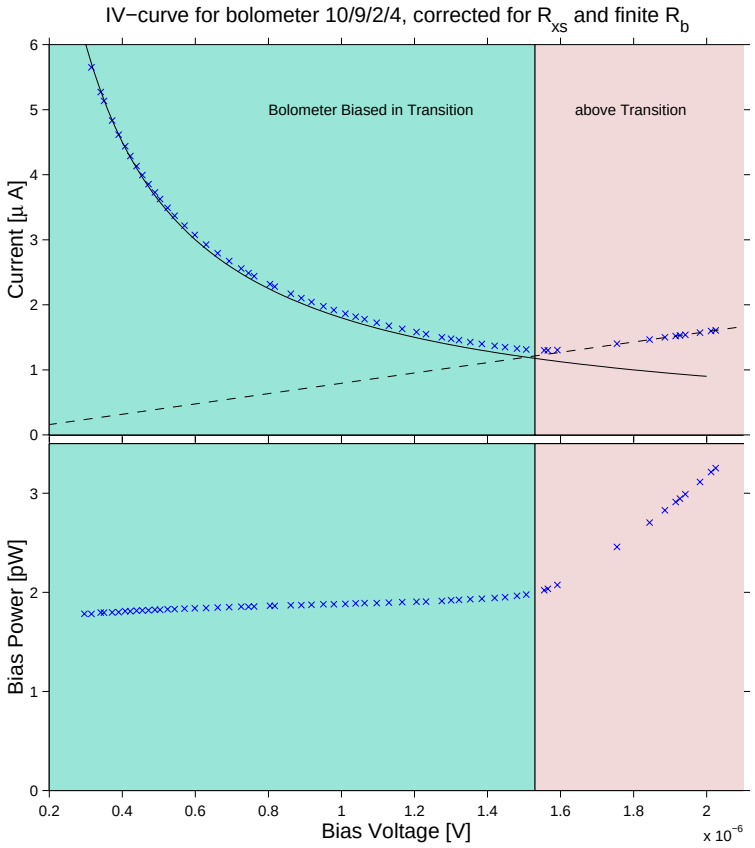

Figure 2.2: This plot shows data from one of the devices described in Chapter 4. In the upper half the current I measured by the SQUID is plotted against the bias voltage V_b. The lower half shows the bias power P_b as a function of V_b. When the bolometer is biased above the superconducting transition it acts as an ohmic resistor and I is proportional to V_b. In the transition, any change in V_b leads to a change in the bolometer resistance R so that approximately $I \propto 1/V_b$ and P_b =const.

Chapter 3

Bolometers for Astronomical Observations

The first section of this chapter discusses the most important considerations entering the design of an absorber-coupled VSB. In section 3.2 we discuss VSBs in a geometry suitable for use in horn-coupled arrays. Finally, in section 3.3 we discuss VSBs in a more compact design allowing the fabrication of arrays to fill the focal plane of a telescope.

3.1 Design of a VSB

3.1.1 General Considerations

A detailed overview over the design of non-superconducting bolometers has been given by Richards [12]. Here we discuss the design of VSBs, which is different in several aspects, particularly because the VSB is a null-detector.

In the design of a VSB for a particular astronomical application many design choices are determined by three parameters:

- the required noise level of the detector
- the expected optical loading on the detector
- the wavelength to be detected

The required noise level of the detector is typically determined by the wavelength to be detected. The criterion is that detector noise should be less than the statistical photon noise (shot noise) arising in the arrival of incoming photons ($NEP = \sqrt{2P_{opt}hc/\lambda}$). The larger λ, the lower the required noise level. In some cases the requirement is relaxed because the noise is dominated by another source, such as atmospheric fluctuations in ground-based experiments.

Expected background loading and required noise level together determine the choice of two fundamental design parameters: the base temperature T_0 at which the bolometer is to be operated and the average thermal conductance $\bar{G}$ of the bolometer. The value of $\bar{G}$ is directly connected to the dynamic thermal conductance G. The relation depends on the nature of the thermal link [13]. If the link is superconducting or insulating it is given by Equation 4.2 below.

A lower boundary for the noise equivalent power (NEP) of thermal fluctuation noise in the thermal link G is set by

$$\gamma\sqrt{4kT_c^2G}, \tag{3.1}$$

where γ is a factor of order unity. Unless there are noise sources unrelated to the bolometer function, thermal fluctuations will dominate the detector noise (cf. Chapter 4) and we get the condition

$$\sqrt{4kT_c^2G} \lesssim \mathrm{NEP}_{required}. \tag{3.2}$$

A good understanding of the expected optical power loading P_{opt} on the bolometer is necessary to choose the correct thermal conductance. If $\bar{G}$ is chosen too small, the bias power P_b will become small resulting in insufficient loop gain, as can be seen from Equation 2.12. In the extreme case $\bar{G}$ ·

$(T_c - T_0) < P_{opt}$ the optical power alone will warm the bolometer above the superconducting transition, even if there is no bias power applied. The bolometer will then show no response and will not be usable.[1] On the other hand, if $\bar{G}$ is chosen too large, the thermal fluctuation noise will be higher than necessary. A typical choice of $\bar{G}$ for a balloon-borne CMB experiment could be

$$\bar{G} \times (T_c - T_0) \approx 3P_{opt,estimated}. \tag{3.3}$$

The ratio of T_c to T_0 is chosen to minimize the noise term 3.1. One finds

$$T_c \approx 1.5 \times T_0. \tag{3.4}$$

We see that, for a given optical power loading and required noise performance, equations 3.2, 3.3, and 3.4 determine the optimal T_0, T_c, and $\bar{G}$. This governs our choice of a refrigeration system, of superconducting materials for the sensor, and, to a certain extent, of materials and designs for the bolometer suspension.

The wavelength λ of the incoming light mainly influences the design of the absorber and of a reflector behind the detector. If the absorber is a mesh,

[1] The VSB is distinct from semiconducting bolometers in this respect. If the power loading rises much above the value for which it was designed, a semiconducting bolometer will still give a response, but will not show optimal performance.

the mesh spacing has to be much smaller than λ so that the absorber effectively acts as a homogeneous surface. Optimal absorption is achieved when a reflector is placed a distance $\lambda/4$ behind the absorber. This is discussed in more detail in Appendix A.

The heat capacity of detector components plays a different role in VSBs than in non-superconducting bolometers. In non-superconducting bolometers the total heat capacity C determines the time constant $\tau \approx C/G$. In some cases, to achieve sufficiently fast response, G has to be increased at the expense of a larger NEP. The VSB, in contrast, is sped up by electrothermal feedback and we find that the time constant is typically not limited by the total heat capacity but rather by the time τ_{abs} it takes the absorber to thermalize internally. This effect can be seen in Figure 3.4. The value of τ_{abs} is determined by the specific heat per unit volume c and the thermal conductivity κ of the materials used for the absorber and underlying structures. It is also dependent on the length of the thermal path in the absorber, as can be seen from Equation 4.1 below. However, for a given λ, this length is usually more or less fixed. The combination of electrothermal feedback and heat capacity distributed in different components of the bolometer can also adversely affect the noise performance, as is discussed extensively in

chapter 4.

3.1.2 Bolometer components

A lithographed VSB typically consists of four different components: the structural elements suspending the bolometer, the absorber for the incoming optical signal, the sensor, and the leads which make contact to the sensor which may include pads for wire bonding. Here we discuss desirable characteristics for the individual components.

Structure

The suspension structure should be light and rigid to shift microphonic resonances to frequencies above the maximum response frequency of the bolometer. The thermal conductance to the heat sink has to be lower than the desired value of G for the bolometer. By using a mesh structure rather than a full membrane the heat capacity can be reduced and the cross section for cosmic ray hits can be minimized. Furthermore, the structure should be robust enough so that the bolometer can be handled conveniently. Structures which allow the close-packing of bolometers into focal plane filling arrays are particularly interesting and are discussed in Section 3.3.

Absorber

To maximize absorption the absorber has to have the right resistance per square. Averaged over areas on the length scale of λ the square resistance should match the impedance of free space of 377Ω. To achieve a low internal thermalization time τ_{abs} a material with a low value of c/κ should be used. By giving the absorber a radial structure the thermal path for a heat signal can be kept to a minimum.

Leads

To properly voltage-bias the sensor, the resistance of the leads has to be much smaller than that of the sensor. Appendix B discusses this in detail. As normal metal leads with such low resistance would show an electronic thermal conductance far exceeding useful values for bolometers, superconducting materials have to be used for the leads. By using a material such as Nb which has a transition temperature far higher than the sensor, the electronic contribution to thermal conductance and heat capacity in the leads can be made negligible. To keep excess resistances small, there should be little or no contact resistance between leads and sensor.

Sensor

The material used for the sensor should show a sharp superconducting transition and the right transition temperature T_c. In particular, it is important that T_c is reproducible from one fabrication batch to the next. It is helpful if the value of T_c can be tuned by varying a fabrication parameter such as the thickness of metal layers in a "proximity sandwich" as discussed in Section 3.2.2. To limit the effect of excess resistances, the sensor should show a normal resistance of $\gtrsim 1\Omega$.

3.1.3 Fabrication process

When we began our work on absorber-coupled VSBs, Bock et al. [14] had recently demonstrated a useful bolometer with an NTD germanium thermistor and a spiderweb geometry. This geometry consists of a sensor in the center of a metallized mesh structure suspended by eight radial legs as can be seen in Figure 3.2. Contact to the sensor is made by leads running along two of the legs. Mesh and legs are made from a 1μm thick membrane of low-stress silicon nitride (LSN). The spiderweb geometry is very rigid, has low heat capacity, a small cross section for cosmic ray hits, and can be made with very low values of G. We used the spiderweb geometry for our work

described in section 3.2. Because the bolometer is suspended by radial legs extending far beyond the absorber, spiderweb bolometers cannot be made in close-packed arrays. In addition, the spiderweb devices are rather fragile and hard to handle. In section 3.3 we discuss an alternative design and fabrication process which overcomes these problems. As Bock et al. did not publish their fabrication process, all processes described in this dissertation were developed by the author.

Once the LSN mesh structure has been released from the underlying Si substrate, it is too fragile to allow coating with photoresist and hence any lithographic processing. It is therefore necessary that the release of the LSN structure is the last fabrication step and that all other structures such as absorber, sensor and leads are fabricated beforehand. All metal structures then have to be protected from damage in the final release step. It turns out that this puts key constraints on the release process.

The most commonly used etch for Si is an aqueous solution of KOH at an elevated temperature ($\approx 80°C$). It is highly anisotropic,[2] stops reliably on LSN and makes it possible to remove large amounts of Si inexpensively. We

[2] At 85°C an aqueous solution of 40 wt% KOH etches along the <100> crystal direction of Si 40 times faster than along the <111> direction [15]. The etch therefore effectively stops on a (111) crystal plane.

attempted to remove the Si substrate underneath the bolometer by etching with KOH from the back side of the wafer. However, when the KOH breaks through the wafer at the end of the etch, it can damage the metal structures on the front of the mesh. We failed to develop a method to protect the metals reliably at this point. Commonly used photoresists are damaged by KOH within seconds. We also experimented with wax, which withstood the KOH for a few minutes but could not be removed completely from the devices afterwards.

The solution to this problem was to release the bolometer by etching the Si from the front side of the wafer with XeF_2 gas [16]. The bulk Si underneath the bolometer can either be removed with KOH beforehand (see Section 3.2.2) or left in place (see Section 3.3.2). The XeF_2 etch is anisotropic and does negligible damage to LSN. The surface of photoresist tends to become very rough in the etch, indicating that the resist is damaged considerably. This effect is most pronounced when the etch rate is very high, presumably because the mesh is heated by reaction heat from the etch. By mixing the XeF_2 gas with inert N_2 gas the etch can be slowed down and the metal structures can be protected by standard photoresist long enough to release the mesh structure. After the etch photoresist can typically not be removed

with liquid solvents such as acetone or commercial photoresist stripper but has to be ashed in an O_2 plasma. Exposure to the O_2 plasma should be kept to a minimum to avoid oxidation of the sensor which can lead to a shift of T_c.

The choice of the material for the sensor depends on the base temperature T_0 at which the system is to be operated, as discussed. The system used for the work described here is cooled with a ^{3}He dilution refrigerator with $T_0 = 264$mK. We therefore looked for a sensor material with $T_c \approx 400$mK. In our first devices we used a single layer of Ti for the sensor and a thick layer of Al on top of the Ti for the leads. This design can be conveniently fabricated because both metals can be deposited in one vacuum step and the standard wet-etch used to pattern the Al stops reliably on Ti without damaging it. In these first devices the Ti sensor showed a $T_c \approx 300$mK and the leads had a transition temperature ≈ 1K. While Ti films can be made with a T_c of 380mK, in practice the transition temperature is often lowered by impurities embedded into the film during the deposition process. Lacking a dedicated deposition system, we found that the T_c of our Ti films were not sufficiently reproducible.

We were able to greatly improve the reproducibility of T_c by fabricating

the sensor as a trilayer sandwich of 500Å of Ti, 400Å of Al, and 500Å of Ti. The transition temperature of such a structure lies between those of the constituent metals. It is determined by the proximity effect between the different layers [17] and can be shifted up or down by varying the individual layer thicknesses. The trilayer structure was chosen to facilitate fabrication. While the upper Ti layer acts as an etch stop for patterning the leads, the lower Ti layer improves adhesion to the underlying LSN. The complete trilayer can be etched in one etch step by Cl-based reactive ion etching (RIE). By making the individual layers relatively thick we limit variations of T_c due to variations in the layer thickness (see [17]). The resulting square resistance of 1.2Ω is adequate for the sensor. Trilayer sensors have proved to be less affected by exposure to an O_2 plasma than Ti sensors. Figure 3.1 shows a typical transition.

Making good contact between the leads and the sensor is another important consideration in the development of a fabrication process. If the metals for leads and sensor are deposited in separate vacuum steps, an oxide layer can form on the metal deposited first causing unacceptable contact resistance between leads and sensor. We have circumvented this problem by depositing all metals in a single vacuum step. The leads therefore consist of a 1000Å

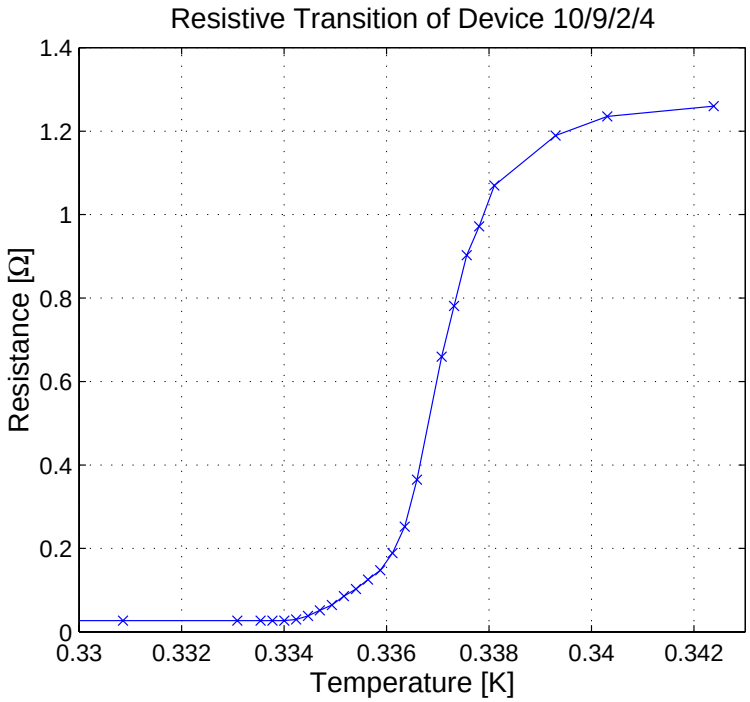

Figure 3.1: The resistive superconducting transition of a sensor made of a trilayer sandwich of 500Å of Ti, 400Å of Al, and 500Å of Ti. Low in the transition ($\approx 300m\Omega$) $\alpha \approx 650$.

thick layer of Al on top of the trilayer. Because the Al is so thick its transition temperature is not significantly shifted by the underlying Ti and the leads show a transition around 1K. The heat capacity and thermal conductance of these leads is relatively high as is discussed in chapter 4. Both could be reduced dramatically by using a single layer of Nb for the leads. We have recently developed a process for making good contact between a Ti/Al sensor and Nb leads deposited in separate vacuum steps [18].

To simplify our fabrication process we chose to make the absorber out of the same material as the sensor. This is possible because the incoming infrared or mm-wave photons are energetic enough to break Cooper-pairs and can be absorbed in the superconducting material. The approach has the disadvantage that the absorber also has unnecessary heat capacity, in particular because it is operated close to its superconducting transition. The value of c/κ which determines τ_{abs} is estimated to be a factor of 200 higher than it would be for a Au absorber.

3.2 Bolometers for Horn-Coupled Arrays

We describe the fabrication and characterization of superconducting transition-edge bolometers for astrophysical applications at far-infrared and mm-wavelengths. The sensor is voltage biased and the current is measured with a SQUID ammeter. Strong negative electrothermal feedback keeps the sensor temperature nearly constant, reduces the response time significantly, and improves linearity. It also makes the responsivity relatively insensitive to changes in optical background loading and refrigerator temperature. The bolometers are made using standard microlithographic techniques suitable for fabrication of large scale horn-coupled arrays. Detailed measurements of optical response are presented for a range of bias conditions and are compared with theory. Measured noise spectra are shown. The material following in sections 3.2.1 to 3.2.4 has been published in Applied Physics Letters [1].

3.2.1 Introduction

Bolometers are the most sensitive detectors of electromagnetic radiation for wavelengths between 200μm and 3mm. Bolometers are used at these wavelengths for laboratory as well as astronomical measurements, for example those of the cosmic microwave background and dust emission from early

(strongly redshifted) galaxies. Arrays of hundreds of sensitive bolometers are needed to instrument more than 10 ground based telescopes in addition to airborne, balloon borne, and space borne instruments.

The voltage-biased superconducting bolometer (VSB) is an attractive new technology for meeting these needs. The entire bolometer structure described here is produced by thin film deposition and optical lithography. This technique is suitable for producing large bolometer arrays. The device employs a voltage-biased superconducting transition-edge sensor [19, 20] and is read out with a SQUID ammeter. The voltage bias results in large negative electrothermal feedback [21]. This makes the device a null detector which has a reduced response time and enhanced linearity. Furthermore, the responsivity is relatively insensitive to changes of optical loading and refrigerator temperature. The noise equivalent power (NEP) can approach the thermal fluctuation limit, due to negligible Johnson noise and the low noise of SQUID ammeters [19, 20]. The large noise margin of the SQUID readout opens the possibility of time multiplexed readouts for large arrays [22].

In previous publications we presented the device concept [19, 23] and tested the device theory with a bolometer prototype [20] which used an electrical heater to simulate infrared radiation. Here we describe the fabrication and

optical characterization of a complete fully lithographed VSB for use with a ^{3}He refrigerator.

3.2.2 Design and Fabrication

The bolometer reported here is supported by a 1μm thick low-stress silicon nitride (LSN) mesh patterned to resemble a spiderweb to reduce the cosmic-ray cross section [14] (see Figure 3.2). The 3.5mm diameter mesh has 7μm wide members and $\approx$ 150μm spaces. The mesh is metallized to absorb far-infrared and mm-waves. It is supported by eight 7μm wide and 1mm long legs which thermally isolate the mesh from the heat sink. The 200μm $\times$ 200μm superconducting thermistor is defined on a continuous region of Si_3N_4 at the center of the mesh. Both the absorber and the thermistor consist of a trilayer of 500Å of Ti, 500Å of Al, and 500Å of Ti. This "proximity sandwich" was chosen to achieve a useful transition temperature of $T_c = 380$mK. The width of the resistive transition was 2.0mK (10%–90%) and the maximum value of $\alpha = d\log R/d\log T$, which measures the steepness of the transition, was 800. In future devices the two upper layers can be removed from the absorber to reduce its heat capacity and to increase its impedance, thereby optimizing the optical efficiency. Superconducting contact to the thermistor is made by

3μm wide leads with $T_c \approx 1$K, which are a sandwich of 1000Å of Al on top of the trilayer. These leads dominate the $\bar{G} = 1.0 \times 10^{-10}$W/K average thermal conductance of the bolometer.

Our bolometers are made entirely by standard microfabrication techniques. A 1μm thick layer of low-stress (non-stoichiometric) silicon nitride is deposited on a standard Si wafer by Low Pressure Chemical Vapor Deposition (LPCVD). Three 500Å and one 1000Å thick layers of Ti, Al, Ti, and Al respectively are deposited in situ by sputter deposition in a system with a base pressure of 10^{-8}torr. All features are defined using a 10:1 reduction wafer stepper and a standard photolithographic process. The leads are defined first and etched with a commercial Al wet etch which stops at the first Ti layer. The absorber and thermistor are defined and etched in a $Cl_2/CHCl_3$ plasma. Square windows are defined on the backside of the wafer and etched into the silicon nitride with an SF_6 plasma. The spiderweb structure is defined on the front and etched by the same process. The photoresist is left in place to protect the devices in a later step. Square windows are etched with aqueous KOH at 67°C into the bulk silicon from the back down to a thickness of 30μm using the LSN as a mask. The wafer is diced and the remaining Si is removed from the individual spiderwebs using a mixture of

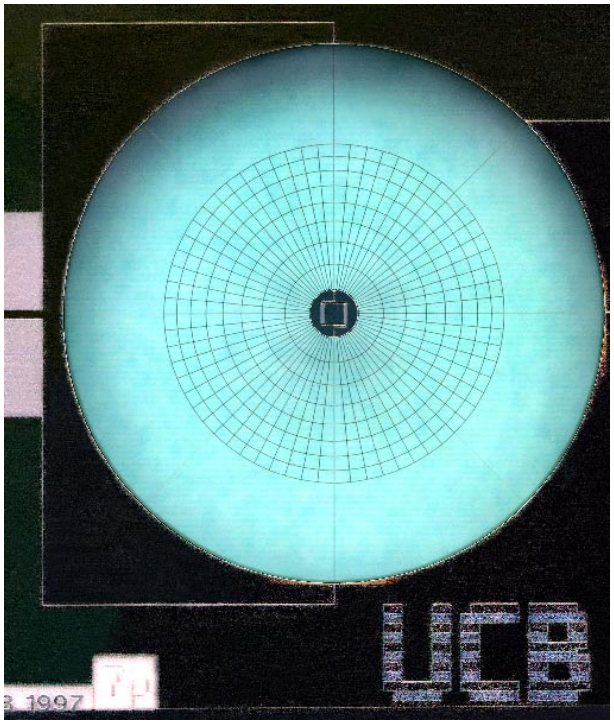

Figure 3.2: Photograph of the fully lithographed bolometer. The circular LSN mesh is metallized to absorb radiation and is supported by eight radial legs. The voltage biased trilayer thermistor is located on a continuous region of membrane in the center and is electrically connected with superconducting leads.

XeF_2 and N_2 gases. The photoresist on the front is ashed in an O_2-plasma and contact to the devices is made with Al wire bonds.

3.2.3 Measurements

These devices were tested in a dark enclosure cooled to $T_0 = 264$mK by a ^{3}He sorption refrigerator. The bolometer has a normal resistance of $R_N = 1.2\Omega$ and was operated at resistances $R \geq 300\text{m}\Omega$. Voltage bias V_b was achieved by current biasing a 20mΩ shunt resistor (Figure 3.3). An unwanted resistance of 27mΩ in series with the bolometer was accounted for in the data analysis. The bolometer current was measured with a SQUID ammeter [24]. An attenuated cold light emitting diode (LED) [25] with λ =626nm was used as an optical stimulator. We estimate that $> 70\%$ of the LED power absorbed in the bolometer was absorbed in the mesh, making the response measurements a valid test for the detection of far-infrared and mm waves which are almost entirely absorbed in the mesh.

The time constant of the VSB was measured from the observed (single exponential) response to a small step in the LED current. The time constant measured when the VSB was biased high on the transition where the feedback is weak was 200ms. This should be close to the intrinsic time constant

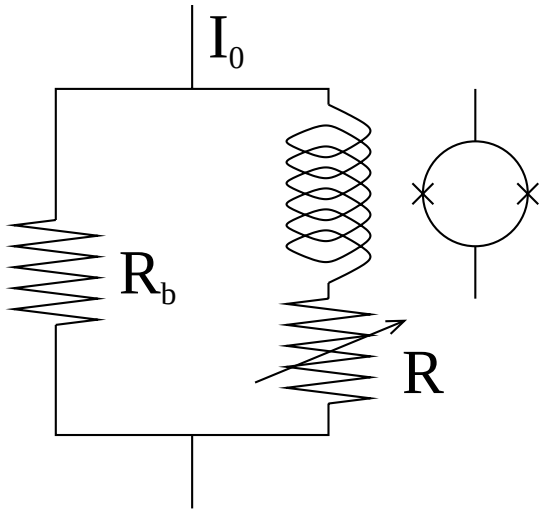

Figure 3.3: The bias circuit used for testing VSBs. The SQUID input coil is connected in series with the bolometer of resistance R. By current biasing a shunt resistor $R_b \ll R$ the bolometer is effectively voltage biased.

$\tau_0 = C/G$ which was estimated from materials properties to be ≈ 350ms. The strength of the electrothermal feedback in a VSB is given by $\mathcal{L} = P_b\alpha/GT_c$ which is referred to as loop gain in analogy to control circuits [20]. Here P_b is the bias power, G is the differential thermal conductance, and T_c is the temperature of the thermistor. When the bias point was moved lower in the transition, the time constant, which is expected [20] to vary as $\tau = \tau_0/(\mathcal{L}+1)$, decreased rapidly as shown in Figure 3.4 until it reached the 13ms time required for heat absorbed in the mesh to reach the thermistor (internal time constant τ_{abs}). The frequency dependence of the optical responsivity S_I was measured using a sinusoidal modulation of the LED current at frequency $\omega/2\pi$. The data in Figure 3.4 (inset) agree with the theoretical prediction $S_I = -(\mathcal{L}/V_b)/(1 + \mathcal{L} + i\omega\tau_0)$.

The bolometer was found to be linear to 2% over a wide range of LED power and then to saturate quickly. This linearity may be limited by that of the LED. The saturation is identified with the optical power $\bar{G}(T_c - T_0) - V_b^2/R_N$, which drives the bolometer out of the transition. This identification calibrates the absorbed power from the LED to $\approx 10\%$ accuracy. This calibration is consistent with the expected low frequency responsivity $S_I = -1/V_b$.

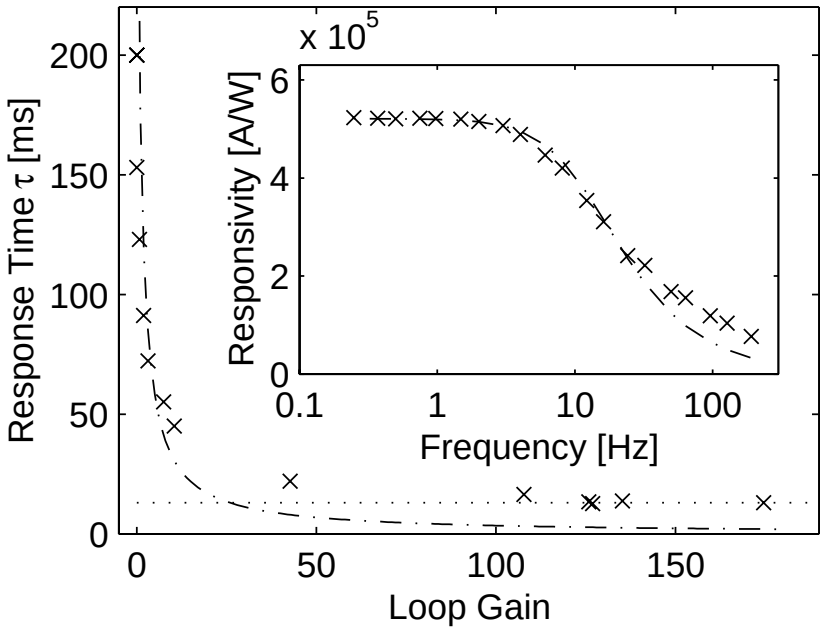

Figure 3.4: Measured response time τ compared with theory (dash-dot line). As expected τ decreases with increasing feedback which is parameterized by the loop gain $\mathcal{L}$. At high gain τ is limited by the internal time constant of the absorber (dotted line). The inset gives a comparison of the measured current responsivity as a function of frequency with theory (dash-dot line). The discrepancy at high frequencies probably arises from light absorbed directly in the thermistor.

Figure 3.5a shows the measured output noise as a function of frequency. Figure 3.5b shows similar results from an earlier spiderweb bolometer [23] with $\bar{G} = 2 \times 10^{-11}$W/K, which had a Ti film thermistor with $R_N = 8\Omega$ and $T_c = 300mK$. At low frequencies in an ideal VSB the noise should be dominated by energy fluctuation noise from the thermal conductance G while Johnson noise is suppressed by electrothermal feedback [19, 20, 13]. At high frequencies Johnson noise from the thermistor should dominate. The SQUID noise is negligible.

Excess noise appears in both devices over a wide frequency range. The noise below ≈3Hz was found to vary with time and with shielding conditions indicating that it was dominated by external sources. At intermediate frequencies $3 < f < 300$Hz a broad noise bump is observed in both devices which is similar to that seen previously [20] in a prototype. In Chapter 4 we introduce a noise model which explains this bump and discuss how the noise performance of future devices can be optimized.

3.2.4 Conclusions

We have built a VSB on a silicon nitride mesh structure using techniques suitable for the fabrication of future detector arrays. The thermistor is a

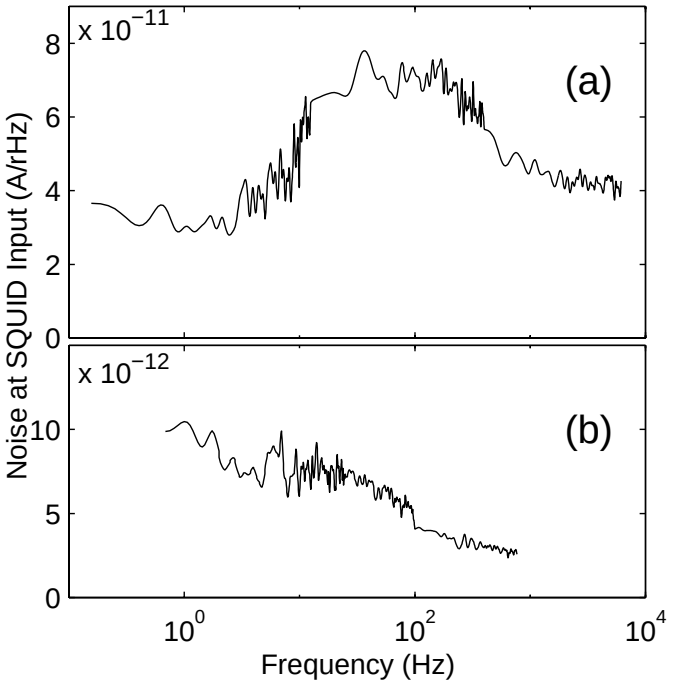

Figure 3.5: Measured noise referred to the SQUID input. (a) for the device described in this paper biased at $R = 409\text{m}\Omega$. (b) for an earlier device with a Ti thermistor biased at $R = 4.25\Omega$. Deduced values of NEP are $8 \times 10^{-17}\text{W}/\sqrt{\text{Hz}}$ at 1Hz for (a) and $1.1 \times 10^{-17}\text{W}/\sqrt{\text{Hz}}$ at 3Hz for (b). These values are 2.5 and 1.3 times the energy fluctuation noise for a bolometer with the value of G employed.

trilayer film whose T_c is determined by proximity effects and can therefore be tuned by varying the individual layer thicknesses. We have demonstrated that the optical time constant is reduced by feedback and the optical responsivity is constant over a wide range in optical power. A broad peak is observed in the noise power spectrum when the bolometer is operated at high gain. The noise can be accounted for by the model presented in Chapter 4.

We thank W. Holmes, B. Cabrera, J. Clarke, M. Hadley, S. Hanany, D. Lieberman, S.W. Nam, and T. Shaw for helpful discussions.

3.3 Focal-Plane Filling Bolometer Arrays

We describe a design for large-format filled arrays of bolometric detectors of infrared and mm-wave radiation produced by standard planar lithography. A square grid of metallized silicon nitride absorbs the radiation. The bolometer suspension, sensor, and wiring occupy a small fraction of the area. We have produced a 1024 element array of fully released and suspended 1.5mm×1.5mm bolometer micro-meshes with a filling factor of 88%. We describe a voltage-biased superconducting bolometer built as a prototype for one array element. We have measured $NEP = 2.3\times10^{-17}\mathrm{W}/\sqrt{\mathrm{Hz}}$, $\tau = 24\mathrm{ms}$, and $G = 2.7\times10^{-11}\mathrm{W/K}$ at 304mK. The material following in sections 3.3.1 to 3.3.4 has been accepted for publication in Applied Physics Letters [2].

3.3.1 Introduction

The far-infrared to mm-wave region is one of the least explored yet one of the most interesting frequency regimes for astrophysics in general and for cosmology in particular. In this wavelength range, scientific progress is tightly tied to the development of better detector technology, specifically to the development of large-format arrays of low-temperature bolometers. Absorber-coupled bolometer arrays currently in use fall significantly short of

filling the diffraction-limited field of view for mm-wave telescopes. In this letter, we describe a new approach for making large-format filled focal plane arrays. Such filled arrays can Nyquist sample (or even oversample) the focal plane and thus the sky. Low-temperature multiplexers are currently being developed [22, 26] to read out the large number of detectors needed to create filled arrays.

Recently, Moseley et al. [27] have presented a "pop up" bolometer design for large-format arrays of voltage-biased superconducting bolometers (VSB) with a high filling factor. One row of devices is made from a single substrate which is subsequently folded so that the mechanical supports and wiring are perpendicular to the plane of the absorber. Agnese et al. [28] have described a different array architecture which is assembled from two wafers by indium bump bonds. There is room for wiring on the lower wafer at the cost of a complicated assembly. They have used this architecture to make large-format arrays of high impedance implanted Si bolometers.

Our design uses a single wafer for simple robust fabrication. As with the Agnese design the mechanical suspension structures and the leads lie in the plane of the absorber and extend only marginally beyond its limits. Our suspension design, however, keeps the mesh under tension and allows us to

use a much thinner, less rigid silicon nitride structure. This makes it possible to manufacture *monolithic* two-dimensional arrays with a high filling factor.

3.3.2 The Prototype Device

Figure 3.6 shows a photograph of our prototype for a single detector element. The absorber is a mesh with a square lattice spacing much smaller than the wavelength to be detected. Mesh absorbers have a low heat capacity and a low cross section for cosmic ray background. They were pioneered by Bock et al. [14] for semiconducting bolometers in a "spiderweb" geometry which is not suitable for making close-packed arrays. Our group has previously produced VSBs in this geometry [1].

We have developed a fabrication method using standard microfabrication techniques that is simpler, results in more robust devices, and gives a higher manufacturing yield than our earlier method [1] for making spiderweb bolometers. A 1μm thick layer of low-stress (non-stoichiometric) silicon nitride (LSN) is deposited on a standard Si wafer by Low Pressure Chemical Vapor Deposition (LPCVD). Four layers of Ti (500Å), Al (400Å), Ti (500Å), and Al (1000Å) are deposited in situ by sputter deposition in a system with a base pressure of 5×10^{-8}torr. All features are defined using a 10:1 reduc-

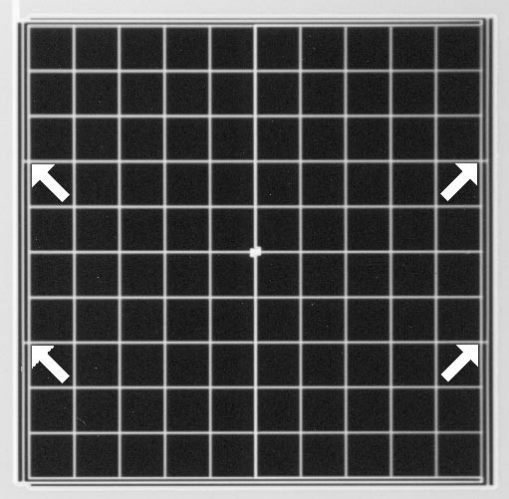

Figure 3.6: The prototype bolometer fills a square area of 1.5mm×1.5mm. It consists of a rigid square grid (light lines) of 11×11 beams, each 7μm wide and metallized for absorption. The grid is suspended at four points (arrows) by 7μm wide free-standing tensioned silicon nitride beams which run along the left and right sides. Two additional beams of silicon nitride run along the top and bottom sides of the grid. They are not under tension and merely serve to support 3μm wide superconducting leads making electric contact to the sensor in the center of the mesh as shown in Figure 3.7. This geometry maximizes the thermal path along the leads and thereby minimizes their contribution to the thermal conductance.

tion wafer stepper and a standard photolithographic process. The leads are defined first and etched with a commercial Al wet etch which stops at the upper Ti layer. The sensor and absorber are defined and etched into the Ti/Al/Ti trilayer with a $Cl_2/CHCl_3$ plasma. This also completes the leads which consist of all four metal layers. The structural elements are defined and etched into the LSN with an SF_6/He plasma. The wafer is diced and the Si is removed from underneath each individual device using XeF_2 gas until the bolometer is freely suspended. The photoresist on the front is ashed in an O_2-plasma and contact to the devices is made with Al wire bonds. As can be seen in Figure 3.7, the absorber mesh is sufficiently rigid to keep its edges, which are not kept under tension by the suspension structure, from curling. As can be seen, the surface of the etched Si shows a roughness on a length scale of $\approx 10\mu$m . We expect this roughness to be averaged over the much larger wavelength of the signal and therefore not to affect optical efficiency.

In a VSB, bias power is dissipated in the sensor, which is biased in the steep part of its resistive superconducting transition. Any change in the absorbed optical power is compensated by a change in bias power. This effect is called strong electrothermal feedback and it makes the bolometer a

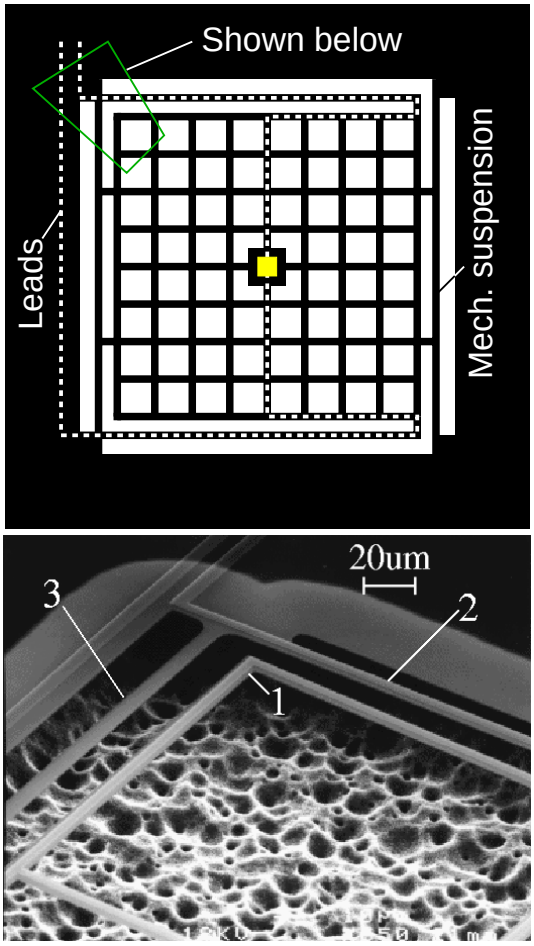

Figure 3.7: Top: A simplified drawing of the mechanical structure of the prototype bolometer. Bottom: A scanning electron micrograph taken at an angle of $\approx 45^{\circ}$ with respect to the bolometer plane shows the corner of the absorber grid (1), one of the leads (2), and one of the suspension structures (3). The rough surface of the Si substrate is due to the XeF_2-etch.

null-detector, increasing its speed and strongly enhancing its linearity [20].

The prototype bolometer was tested in a dark enclosure cooled to $T_0 = 264$mK by a ^{3}He sorption refrigerator. The Ti/Al/Ti sensor has a normal resistance of $R_N = 1.3\Omega$ and shows a resistive transition at $T_c = 304$mK with the maximum transition steepness $\alpha = d\log R/d\log T$ of 740. The maximum value of the loop gain, which is a measure of the strength of the feedback, was estimated to be $\mathcal{L} \approx 50$. In future devices the proximity effect trilayer can be optimized to give $T_c \approx 1.5 \times T_0 = 400$mK for best sensitivity and $\mathcal{L} > 200$.

Voltage bias was achieved by current biasing a 20mΩ shunt resistor. An unwanted resistance of 15mΩ in series with the device was accounted for in the data analysis. The bolometer current was measured with a commercial SQUID ammeter [24]. Noise spectra were measured with a spectrum analyzer [29]. An attenuated cold light-emitting diode [25] with λ =626nm was used as an optical stimulator. The power emitted by the diode was stepped up abruptly and the resulting change in the bolometer output was fitted to an exponential to determine the bolometer time constant.

The average thermal conductance was found to be $G = 2.7 \times 10^{-11}$W/K. We estimate that half of this conductance is due to the leads. Figure 3.8

shows the noise equivalent power when the device is biased at a resistance of 80mΩ. The measured noise level is close to the fundamental limit $\sqrt{4k_BT^2G}$ set by simple thermal fluctuation theory. The rise in the noise spectrum above 3Hz can be explained with a more complicated thermal model which will be published elsewhere [3]. The $1/f$ knee at 300mHz is higher than expected from SQUID noise alone and is possibly caused by the cryogenic system.

Without electrothermal feedback, the time-constant of the bolometer was measured to be $\tau_0 = 127$ms. From this value we estimate the total heat capacity to be 3.2×10^{-12}J/K, which is in good agreement with prediction based on materials parameters. Electrothermal feedback reduces the time-constant [19] to $\tau = \tau_0/(\mathcal{L}+1)$ unless it is limited by an internal thermalization time τ_i of the absorber. We measure $\tau_i = 24$ms. Our noise model shows [3] that it is necessary to reduce the heat capacities of the electrical leads and of the absorber to optimize the noise-performance. This can best be done by using different materials for leads and absorber. We have already successfully used Nb as a lead material on LSN (see Chapter 5). Because of its high superconducting transition temperature ≈ 9K it should have negligible heat capacity and thermal conductance at the operating temperature of our devices. Using

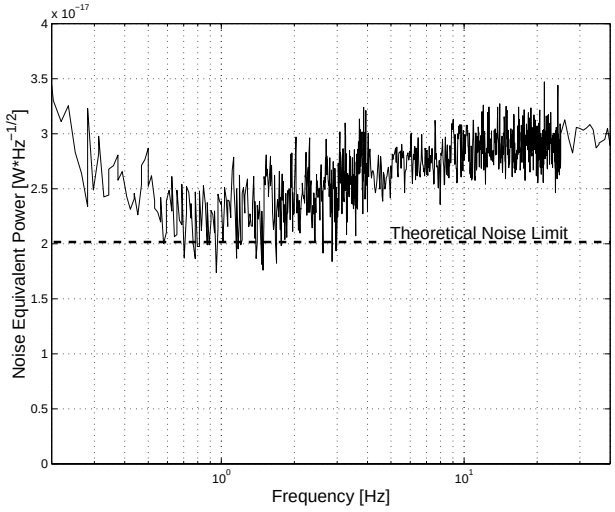

Figure 3.8: Noise equivalent power when the device is biased at $R = 80\text{m}\Omega$.

Au for the absorber would also reduce the present heat capacity considerably. Au-absorbers with internal thermalization times as low as 4.5ms have been demonstrated [30].

We predict that a device with the described structure with Nb leads and an Au absorber would show white noise at the limit set by simple thermal fluctuation theory up to 300Hz. At temperatures around 400mK, Nb leads would not contribute appreciably to the thermal conductance. The current design would then give $G \approx 1.3 \times 10^{-11}$W/K and NEP $< 10^{-17}$W/$\sqrt{\text{Hz}}$, suitable for single-mode ground-based photometry from the best sites. Values as low as $G \approx 4 \times 10^{-12}$W/K could be achieved by using a thinner LSN film and narrower structures. If the bolometer was operated at $T_0 = 100$mK, G would be reduced by a further factor ≈ 10. The resulting NEP $< 10^{-18}$W/$\sqrt{\text{Hz}}$ would be adequate for single-mode photometry from an ideal cooled space-borne telescope which is background-limited by emission from galactic dust.

The low thermal conductance of Nb-leads would also allow us to run them directly along the mechanical support. This would make it possible to omit the structures currently supporting the leads and to suspend the bolometer mesh on all four sides, making the design even more rigid (see Figure 3.9).

To optimize the coupling of the signal to the absorber a reflective layer

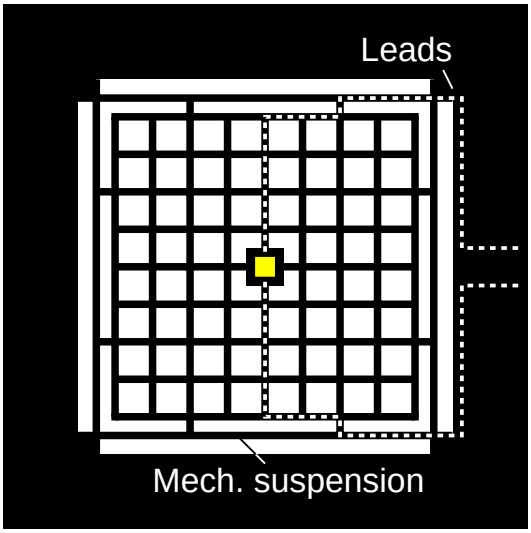

Figure 3.9: By suspending the bolometer on all four sides the structure would be made even more rigid. Nb leads running along the suspension would make a negligible contribution to the thermal conductance.

(e.g. Al) will be deposited on the back of future devices so that there is a gap of thickness a and a Si layer of thickness b between the absorber and the reflector (see Figure 3.10). The Si behind the bolometer must be thinned in a controlled way as can be done with silicon on insulator (SOI) wafers and trench etching techniques.[31]

The optimal values of a and b depend on the wavelength λ of the signal. Our calculations show that for any $a < \lambda/4$ there is a value for b such that absorptivity is unity (see Appendix A for details). A deviation of 10% from the optimal value of b translates into a reduction of the absorptivity by $\approx 2\%$. We find that the parameter b is uniform within the measurement accuracy given by the roughness of the etched Si surface. In a 32×32 element array we observe overetching of the elements at the very edge of the array. We expect to eliminate this problem by modifying the gas flow pattern in the etch apparatus. This should make it possible to produce arrays for wavelengths from $\approx 250\mu$m to several mm with this approach. For shorter wavelengths one would etch away all the Si remaining underneath the bolometer, opening a window to the back of the wafer. A metal coated Si surface micromachined from another SOI wafer can then be brought in from the back to create a reflector precisely $\lambda/4$ behind the absorber, as shown in Figure 3.11.

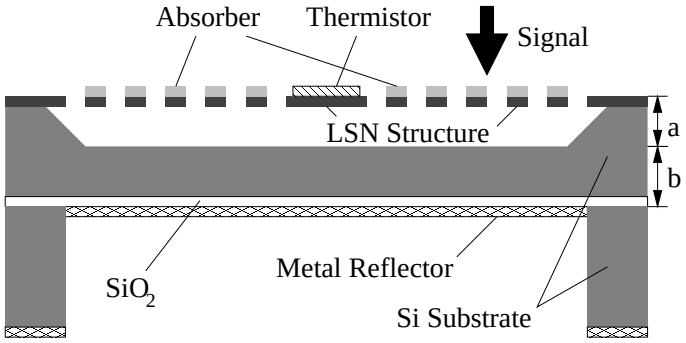

Figure 3.10: Cross section of an individual bolometer with back reflector. The vertical scale has been exaggerated.

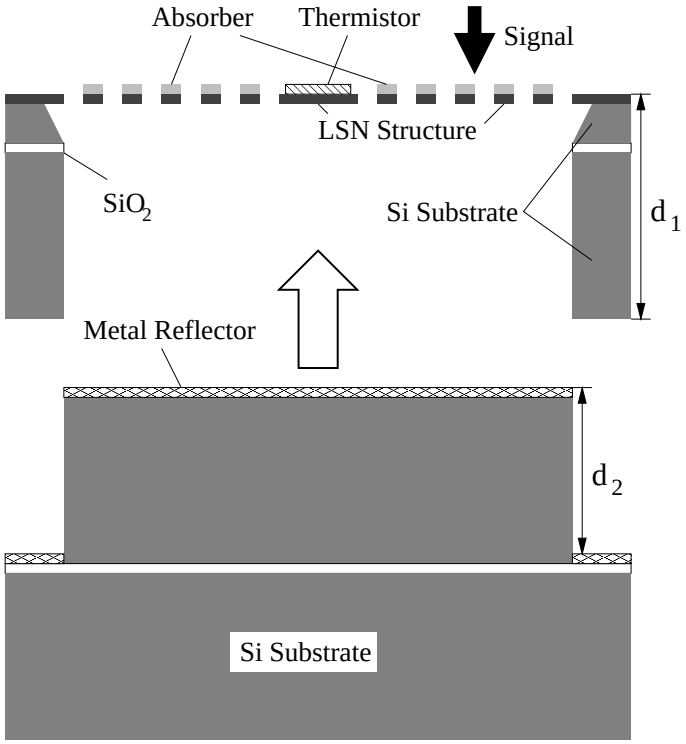

Figure 3.11: Cross section of an alternative design in which the reflector is fabricated on a separate SOI wafer such that $d_1 - d_2 = \lambda/4$. The vertical scale has been exaggerated.

3.3.3 Monolithic Bolometer Arrays

To explore the feasibility of large arrays, we have manufactured LSN structures for arrays of 4×4, 8×8, and 32×32 bolometers. Figure 3.12 shows the LSN structure for a 32×32 element array covered with a 500Å thick layer of Ti to facilitate photography. The production yield is excellent and all 1024 meshes are intact. Ten of them show defects which are clearly due to dust contamination. Our devices are made in a class-100 cleanroom facility and a cleaner environment will be necessary to make flawless large-scale arrays. The structures are much more robust than the spiderweb bolometers made previously [1] because they are protected by the Si substrate. The spacing between the bolometers was chosen such that contact to all devices can be made with 1μm wide leads and a 1μm spacing between leads. The absorbers fill 88% of the area.

The meshes in the arrays show a tendency to curl in the areas extending beyond the suspension points. This effect was not seen in our complete prototype bolometers. It could be due to the different metallization or a different degree of stress in the batch of LSN used for making the arrays. While the proposed suspension on all four sides would most likely remedy this problem, further investigation of the issue is necessary.

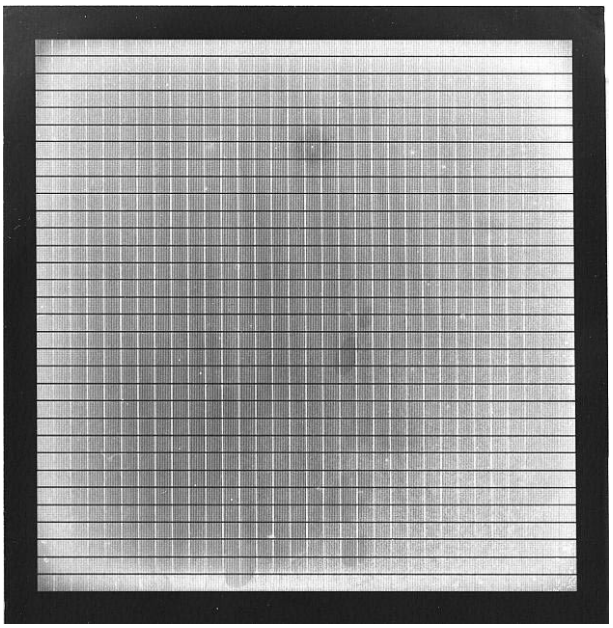

Figure 3.12: This photograph shows the silicon nitride structure for a 1024 element array of 1.5mm×1.5mm bolometers.

3.3.4 Conclusions

In summary, we have described a new bolometer design which allows the production of large monolithic detector arrays with a very high filling factor by standard planar lithography. We have produced a prototype bolometer operating close to the fundamental noise limit and indicated changes necessary to produce optimized bolometers. There appear to be no major obstacles to the fabrication of large-format filled arrays of VSBs for $200\mu\text{m} \leq \lambda \leq 3\text{mm}$ with values for G as low as $4 \times 10^{-12}\text{W/K}$ for $T_0 = 264\text{mK}$ and $4 \times 10^{-13}\text{W/K}$ for $T_0 = 100\text{mK}$. Arrays for $\lambda < 200\mu\text{m}$ can be fabricated with reflectors made on a separate wafer.

We thank J. Bustillo for suggesting the use of SOI wafers in future fabrication.

Chapter 4

A Model for the Noise

We are developing superconducting transition-edge bolometers for far-infrared and millimeter wavelengths. The bolometers described here are suspended by thin legs of silicon nitride for thermal isolation. At frequencies between 200mHz and 10-50Hz, these devices show white noise at their thermal fluctuation limit ($NEP \approx 10^{-17}\mathrm{W}/\sqrt{\mathrm{Hz}}$). At higher frequencies a broad peak appears in the noise spectrum which we attribute to a combination of thermal fluctuations in complex thermal circuits and electrothermal feedback. Detailed noise calculations fit the noise measured in three different devices which were specifically designed to test the model. We discuss how changes in bolometer materials can shift the noise peak above the frequency

range of interest for most applications. The material following in Sections 4.1 to 4.4 has been submitted for publication in Applied Optics [3].

4.1 Introduction

Bolometers are the most sensitive direct detectors of electromagnetic radiation for wavelengths between 200μm and 3mm. Bolometers are used at these wavelengths for laboratory measurements and for astrophysical observations, such as measurements of the cosmic microwave background and emission from galactic and extragalactic dust. Large arrays of $10^3 - 10^4$ bolometers are planned which would give a substantial increase in performance compared to current arrays for ground-based, airborne, balloon-borne, and space-borne observatories.

The voltage-biased superconducting bolometer (VSB) is an attractive technology for building such arrays. It employs a voltage-biased transition-edge sensor and is read out with a superconducting quantum interference device (SQUID) ammeter [19]. The bias power dissipated in the voltage-biased sensor compensates for any changes in the absorbed optical power [21]. This effect, called negative electrothermal feedback, makes the device a

null detector which is linear over a wide range of signal power. Electrothermal feedback with loop gain $\mathcal{L}$ reduces the response time by a factor $\mathcal{L}+1$. The detailed theory of device response is given elsewhere [20]. The VSB is relatively immune to changes in environmental factors such as background loading and heat sink temperature, is compatible with output multiplexers [26, 22], and can be made by standard lithography.

We have previously reported on a suspended VSB made entirely by thin film lithography [1]. The 200μm $\times 200\mu$m thermistor is in the center of a 3.5mm diameter circular mesh of 1μm thick low-stress (non-stoichiometric) silicon nitride (LSN). This "spiderweb" mesh is suspended by eight 1mm long LSN legs and supports an absorbing metal film which is thermally connected to the thermistor. These spiderweb devices, as well as new devices reported here, have 1/f noise below $\approx$ 200mHz and white noise up to 4-20Hz. At higher frequencies we observe a wide noise peak rising to nearly twice the white noise level as shown in Figure 4.1. This peak is seen in devices with very different heat capacities and thermal conductances and has been observed by at least one other group [32].

A fundamental limit for the noise in a bolometer is set by thermal fluctuations in a simple thermal circuit consisting of a single heat capacity and a

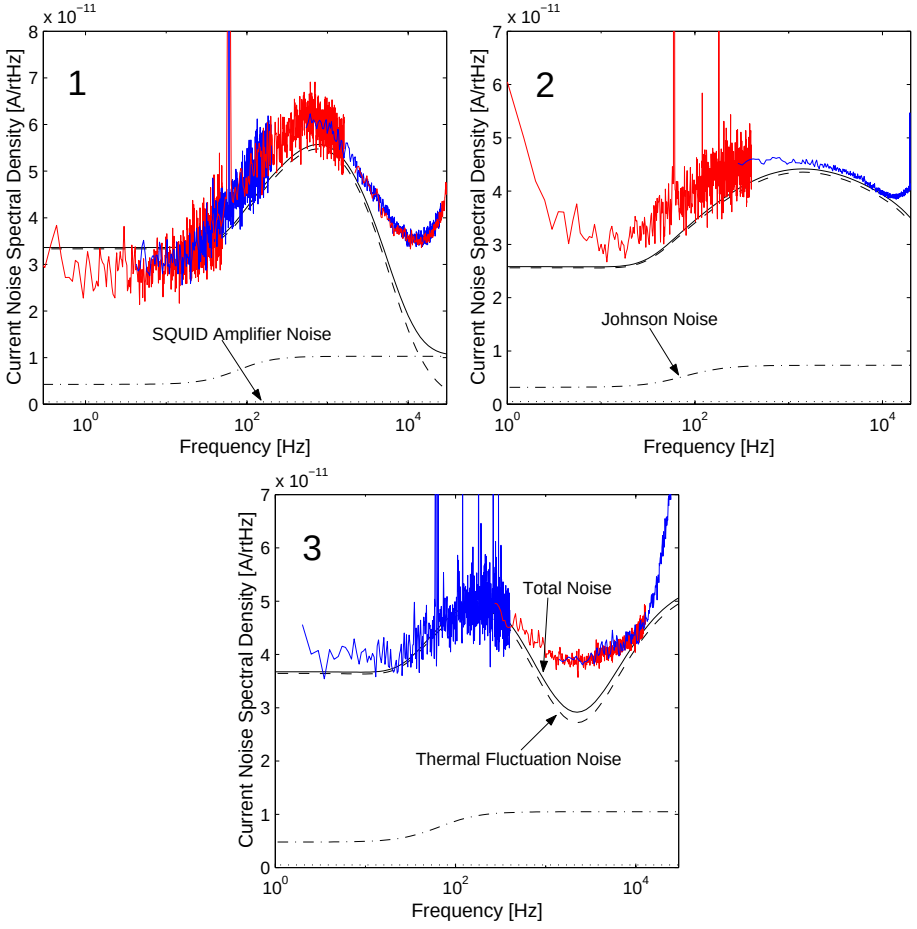

Figure 4.1: Output current noise spectral density for devices 1, 2, and 3 biased at 136mΩ, 259mΩ, and 126mΩ, respectively. Noise spectra measured at different frequencies were combined to cover the full range of frequencies. The onset of low frequency $(1/f)$ noise in these devices is generally below 300mHz. Higher onsets seen for devices 2 and 3 are due to a malfunction of the bias circuit. The rise in noise observed above 20kHz in all devices is due to a resonance in the SQUID system. The total noise is the quadrature sum of the thermal fluctuation noise predicted by our model, SQUID noise, and Johnson noise.

single thermal link to a temperature reservoir (see Figure 2.1). When referred to the bolometer output the thermal fluctuation noise power spectrum is flat at low frequencies and rolls off at the maximum response frequency of the bolometer. This model correctly predicts the white noise level in our devices, but not the noise peak at higher frequencies. To create bolometers with optimal noise performance at higher response frequencies it proved necessary to determine the mechanism for the additional noise peak and to understand how it is influenced by design parameters. The goal is to eliminate the peak or to shift it above the range of frequencies in which the bolometer is to be used.

We have created more complex thermal models with two or three lumped heat capacities connected in series by thermal conductances which are a better representation of the leads, thermistor, and radiation absorber in our bolometers. These models predict a noise peak which arises from the interaction of electrothermal feedback with the thermal circuit. However, the quantitative agreement with measurements on our devices is poor.

Most absorber-coupled or suspended bolometers have distributed thermal circuits which are only approximately described by these models. A simple estimate can be used to determine whether a particular component

can be treated as a lumped thermal object. In one dimension, a heat pulse propagates a distance l in a characteristic time

$$\tau = l^2 c/\kappa \tag{4.1}$$

where c is the heat capacity per unit volume and κ is the thermal conductivity. This implies that if we want to determine the noise performance of a bolometer at frequency f we can only treat those elements as lumped heat capacities which have characteristic dimensions smaller than $l = \sqrt{\kappa/2\pi f c}$.

Using this criterion, some elements of our devices cannot be treated as lumped heat capacities. In the following we introduce a detailed thermal model taking into account the distributed heat capacities and thermal conductances of the electric leads, absorber, and supporting membrane as well as the lumped heat capacity of the thermistor. This model predicts a peak in the noise spectra of our spiderweb devices. However, this does not provide a rigorous test of the model since the heat capacities and thermal conductances of the individual elements in such bolometers are not accurately known. For a more rigorous test of our thermal model we have built and characterized simpler devices with a range of thermal parameters. These parameters can be estimated accurately and we find good agreement between the model and data from these test devices.

Previously, we considered an alternative noise model based on thermal fluctuations inside the sensor [1]. Detailed comparison with the current data shows that it cannot explain the dominant noise features observed in our test devices.

4.2 Fabrication and Experiment

To test the thermal noise model, we fabricated simple devices with a thermistor, a suspension to thermally insulate the thermistor from the substrate, and electrical leads making contact to the thermistor. The absorber was omitted and the mechanical structure was kept to a minimum. The LSN structure used for suspension resembles an elongated letter 'H' as shown in Figure 4.2. The four legs are each 7μm wide and 1640μm long. The small square in the center is 60μm on a side. The thermistor is patterned on this square and superconducting leads run along the two legs on the left.

The devices are made entirely by standard microfabrication techniques. A 1μm thick layer of LSN is deposited on a standard Si wafer by Low Pressure Chemical Vapor Deposition (LPCVD). Layers of Ti (500Å), Al (400Å), Ti (500Å), and Al (1000Å) are successively deposited *in situ* by sputter deposi-

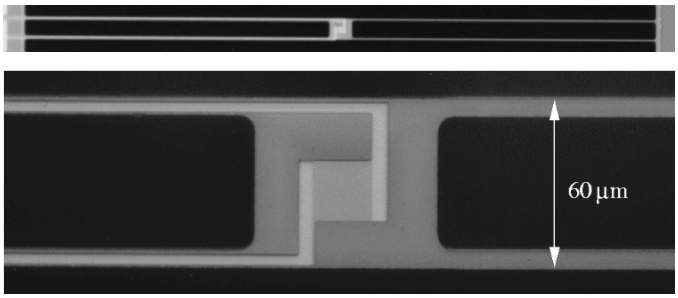

Figure 4.2: The upper photograph shows one of the test-devices. The thermistor is in the center. The support legs extend to the left and right. The lower photograph shows a magnified image of the thermistor. The suspension structure is made from a 1μm thick film of low-stress silicon nitride. Superconducting leads along the two legs on the left make contact to the sensor. The four legs are each 7μm wide and 1640μm long.

tion in a system with a base pressure of 5×10^{-8}torr. All features are defined using a 10:1 reduction wafer stepper and a standard photolithographic process. The leads are masked with photoresist and the wafer is etched with a commercial Al wet etch which stops at the upper Ti layer. Then the thermistor is masked and the remaining Ti/Al/Ti trilayer is etched in a $Cl_2/CHCl_3$ plasma. This also completes the leads which consist of all four metal layers. The H-structure is then masked and the LSN is etched with an SF_6/He plasma. Finally, the wafer is diced and the Si is removed from underneath the individual device using XeF_2 gas until the structure is freely suspended by the four legs. The photoresist on the front is ashed in an O_2-plasma and contact to the devices is made with Al wire bonds. This fabrication process does not require the removal of the entire Si substrate underneath the device. It produces robust devices which can be handled conveniently and has a very high production yield. All of the hundreds of devices we have produced were structurally intact. Complete bolometers with absorbers have also been fabricated by this method and have been reported elsewhere [2].

The approach of making the leads out of the superconducting Ti/Al/Ti/Al quadralayer was chosen to simplify fabrication. It has the disadvantage that the leads are rather thick and their $T_c \approx 1$K is not far above

the operating temperature of ≈ 0.33K. Making the leads out of a thin layer of a material with higher T_c, such as Nb, would significantly reduce their heat capacity.

We report on three devices which differ in the width of their leads and the size of their thermistors, resulting in different distributions of their total heat capacity. Table 4.2 summarizes the design parameters. The transition temperature T_c of the Ti/Al/Ti thermistors, like that of the leads, is determined by the proximity effect and can be changed by varying the layer thicknesses of the individual metals. The thermistors have a normal resistance of $R_N = 1.3\Omega$. The parameter $\alpha = d\log R/d\log T$ is a measure of the steepness of the superconducting transition. Device 3 has a piece of the trilayer with an area of $5000(\mu\text{m})^2$ thermally attached to the thermistor to simulate the added heat capacity of an optical absorber.

The devices were tested in a dark enclosure cooled to $T_0 = 264$mK by a ^{3}He sorption refrigerator. Voltage bias $V_b \approx 500$nV was achieved by current biasing a 20mΩ shunt resistor. Parasitic resistances of order 10mΩ in series with the devices were accounted for in the data analysis. The bolometer current was measured with a SQUID ammeter [24] and noise spectra were computed with a spectrum analyzer [29]. An attenuated cold light-emitting

	thermistor	leads	measured	T_c	α	C_{total}	fractional heat capacity		
							leads	therm.	abs.
#	size	width	$\bar{G}$ [W/K]	[mK]	(max.)	[J/K]			
1	50μm $\times 50\mu$m	2μm	2.6×10^{-11}	337	650	1.1×10^{-12}	90.3%	9.7%	-
2	20μm $\times 20\mu$m	3μm	3.4×10^{-11}	334	300	2.0×10^{-12}	99.1%	0.9%	-
3	10μm $\times 10\mu$m	3μm	3.0×10^{-11}	326	710	2.3×10^{-12}	86.6%	0.2%	13.2%

Table 4.1: Parameters of the three test-devices. The measured values of $\bar{G}$ are in good agreement with predictions from materials parameters and with previous measurements.

diode [25] with λ =626nm was used as an optical stimulator for time-constant measurements. The power emitted by the diode was stepped up abruptly and the resulting change in the bolometer output was fitted to an exponential to determine the time constant.

Figure 4.1 shows noise data from the three devices. The current spectral density referred to the SQUID input is plotted as a function of frequency. Low-frequency ($1/f$) noise drops off below 300mHz. Up to $\approx$ 20Hz the white noise plateaus at about the level of ideal thermal fluctuation noise. At higher frequencies a wide peak appears in the spectrum. At very high frequencies the noise level rises again. This is due to a resonance in the SQUID system which is not related to our devices.

4.3 Analysis and Modeling

We now discuss how the physical parameters of simple and distributed bolometers can be estimated and describe our thermal model for distributed bolometers. We represent the model system of heat capacities and thermal conductances with a matrix, introduce a term representing the electrothermal feedback, and calculate the response of the system to thermal fluctuation

noise including correlations between the noise terms.

To make an accurate thermal model of a simple bolometer it is necessary to know the total heat capacity C and the average thermal conductance $\bar{G}$ between the thermistor and the heat sink. The parameter $\bar{G}$ can be measured directly from the bias power $P_b = V_b I$. When the bolometer is biased in the transition and no optical power is incident $\bar{G} = P_b/(T_c - T_0)$. For superconducting leads, the average thermal conductance is proportional to T^3 and the differential thermal conductance $G = dP_b/dT$ is given by [19]

$$G = 4\bar{G}(1 - T_0/T_c)/(1 - {T_0}^4/{T_c}^4). \tag{4.2}$$

The heat capacity C must be inferred from time-constant measurements. For a simple bolometer without electrothermal feedback, in which the heat capacity of the thermal link between the thermistor and heat sink is negligible, the observed time constant is $\tau_0 = C/G$ [12].

In our test-devices, however, most of the heat capacity is distributed evenly along the leads between the heat sink and thermistor. The thermistor and, in device 3, the absorber are expected to have a heat capacity per unit area similar to that of the leads but have a much smaller area (see Table 4.2). The LSN structure is in intimate contact with the metal films. Its contribution to thermal conductivity and heat capacity can be taken into account by

adjusting these parameters for the metal films accordingly. In our case, the contribution is negligible. We model the leads as a chain of identical lumped heat capacities C_1 through C_N and thermal conductances G_1 through G_{N+1} connecting the heat sink with constant temperature T_0 with the thermistor C_{N+1}, as shown in Figure 4.3. A value for C_{N+1} is estimated from materials parameters. For device 3, values for the lumped heat capacity of the absorber C_{N+2} and its thermal link to the thermistor G_{N+2} are also estimated from materials parameters and the assumption $T_{N+2} = T_{N+1}$ is made. If we consider the steady-state response, we can obtain a self-consistent set of values $\{G_1, T_1, \ldots, G_{N+2}, T_{N+2}\}$ satisfying the conditions $1/\bar{G} = \sum_{i=1}^{N+1} 1/G_i$, $P_b = G_i(T_i - T_{i-1})$ for all i, and $G_i \propto {T_i}^3$ for all i.

If the temperature of the thermistor T_{N+1} changes, T_N will follow this change almost completely while T_1 will stay largely unaffected. Consequently, the C_i close to the heat sink will contribute less to the measured response time than those close to the thermistor and $\tau_0 < \sum_{i=1}^{N+1} C_i/\bar{G}$.

To measure τ_0 rather than the reduced time constant $\tau = \tau_0/(\mathcal{L}+1)$ in the VSB, we bias the device on the upper end of the transition where $\mathcal{L} \ll 1$. The device is then no longer a null-detector and the temperatures of leads and thermistor do not remain constant when the optical power is changed.

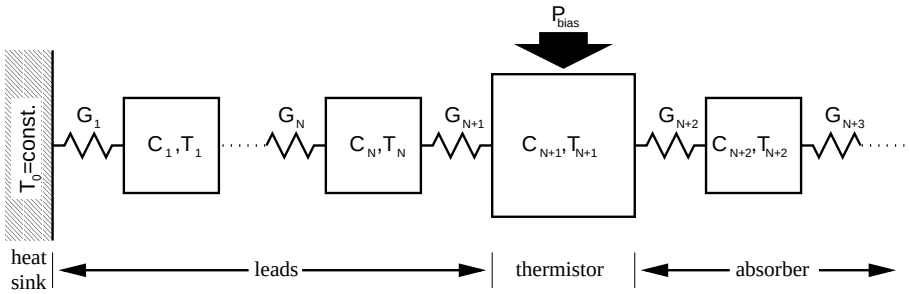

Figure 4.3: The thermal circuit used for our noise calculations. Leads, thermistor, and absorber are modeled as a chain of many heat capacities connected by thermal links.

This fact makes it necessary to take into account an additional effect in the determination of the total heat capacity C. The thermal conductance along the leads depends on their temperature. Since $dG_i/dT_i > 0$, changes in optical power are partially compensated. This effect is distinct from the electrothermal feedback in the thermistor discussed earlier, although it also shortens the observed response time.

To determine the correct value of the total heat capacity $C = \sum_{i=1}^{N+1} C_i$ of devices 1 and 2 we numerically simulate the evolution of the variables T_1 through T_{N+1} and G_1 through G_{N+1} after an abrupt step in the absorbed optical power. This can be done with a program which calculates the power flowing through each of the thermal links G_i in sufficiently small time steps $\Delta t \ll C_i/G_i$ and adjusts the values for the T_i and G_i accordingly after each step. The value for C is then chosen so that the time constant with which the thermistor-temperature T_{N+1} changes after a change in incident optical power matches the observed τ_0 of the device. We find heat capacities which are a factor 2.4 and 4.0 higher than those estimated from materials properties for devices 1 and 2, respectively. For device 3, measurements of τ_0 were not conclusive, but the leads are nominally identical to those of device 2 and we assume the same value for their heat capacity. We have observed

such excess heat capacities in earlier devices and they have also been seen by at least one other group [33]. In that case, excess heat capacities have been attributed to thin films of organic residue from the fabrication process. Spectroscopic analysis [34] shows that our devices contain $> 1\%$ of C and F by mass. Further work is required to determine whether this is the origin of the observed excess heat capacity.

Having determined values for $C_1 \ldots C_{N+1}$ and $G_1 \ldots G_{N+1}$ we can now model the thermal behavior of the device. The goal is to understand how thermal fluctuations at any point in the system will be reflected in T_{N+1}. Since $I = V_b/R$ and $R = R(T_{N+1})$, this then determines the effect of such fluctuations on the current I measured by the SQUID. Here we give a derivation for the general case of $N + 1$ heat capacities. To make our calculations more transparent, we give a more explicit derivation of the case $N = 1$ in Appendix C.

An arbitrarily complicated thermal circuit with Z thermal masses can be represented by a $Z \times Z$ thermal matrix M [35]. The temperature response of the system to small changes in the power fed into the thermal masses 1 to Z is given by

$$\begin{pmatrix} dT_1 \\ \vdots \\ dT_Z \end{pmatrix} = M^{-1} \times \begin{pmatrix} dP_1 \\ \vdots \\ dP_Z \end{pmatrix}. \tag{4.3}$$

In our case only neighboring thermal masses are directly connected thermally, so only elements near the diagonal of M are non-zero:

$$M = \begin{pmatrix} i\omega C_1 + G_1 + G_2 & -G_2 & 0 & \cdots & 0 \\ -G_2 & i\omega C_2 + G_2 + G_3 & -G_3 & \cdots & 0 \\ 0 & -G_3 & i\omega C_3 + G_3 + G_4 & \cdots & 0 \\ \vdots & \vdots & \vdots & \ddots & \vdots \\ 0 & 0 & 0 & \cdots & i\omega C_{N+1} + G_{N+1} \end{pmatrix}. \tag{4.4}$$

In the case of device 3, M has an additional row and column to include C_{N+2} and G_{N+2}.

Every thermal mass C_1 through C_N sees noise power $P_{i,i}$ arising from thermal fluctuations in the thermal link G_i to its left and $P_{i,i+1}$ from thermal fluctuations in the thermal link G_{i+1} to its right. C_{N+1} sees one such term in addition to the bias power P_b, so that

$$\begin{pmatrix} dP_{1,1} + dP_{1,2} \\ \vdots \\ dP_{N,N} + dP_{N,N+1} \\ dP_b + dP_{N+1,N+1} \end{pmatrix} = M \times \begin{pmatrix} dT_1 \\ \vdots \\ dT_N \\ dT_{N+1} \end{pmatrix}. \tag{4.5}$$

The bias power absorbed in C_{N+1} is determined by the temperature of the thermistor T_{N+1}. We write

$$P_b = \frac{{V_b}^2}{R(T_{N+1})} \Rightarrow \frac{dP_b}{dT_{N+1}} = \frac{-{V_b}^2}{R^2} \times \frac{dR}{dT_{N+1}} = \frac{-P_b\alpha}{T_{N+1}}. \tag{4.6}$$

We can eliminate the term dP_b from the left side of equation (4.5) by replacing the matrix M with

$$M' = M + \begin{pmatrix} 0 & \cdots & 0 \\ \vdots & \ddots & \vdots \\ 0 & \cdots & P_b\alpha/T_{N+1} \end{pmatrix}. \tag{4.7}$$

We can solve equation (4.5) for dT_{N+1} by inverting the matrix M'. For large N this is best done numerically.[1] The change in thermistor temperature is

$$dT_{N+1} = \sum_{i=1}^{N} q_i \times (dP_{i,i} + dP_{i,i+1}) + q_{N+1} dP_{N+1,N+1}, \tag{4.8}$$

[1]Since the matrix M' is filled mostly with zeros, it can be inverted easily even for values of N of several hundred.

where the q_i are elements of $(M')^{-1}$. The spectral density of fluctuations of T_{N+1} is then

$$\begin{aligned} ST_{N+1} &= \sum_{i=1}^{N} \mid q_i \mid^2 \times (SN_{i,i} + SN_{i,i+1}) \\ &+ \mid q_{N+1} \mid^2 \times SN_{N+1,N+1} + 2 \times \sum_{i=1}^{N} \mid q_i q_{i+1} \mid \times SC_i. \end{aligned} \tag{4.9}$$

Here $SN_{i,j}$ is the power spectral density arising in C_i from the arrival and departure of quantized carriers of energy (electrons or phonons) through the thermal link G_j. This noise has a white spectrum and is seen by the thermal masses on both ends of G_j:

$$SN_{i,i} = SN_{i-1,i} = 4k_B {T_i}^2 G_i \gamma, \tag{4.10}$$

where for a superconductor $\gamma = \frac{4}{9} \times \left(1 - (T_i/T_{i-1})^9\right) / \left(1 - (T_i/T_{i-1})^4\right)$ [13]. The last term of equation (4.9) takes into account correlations between the noise spectral densities observed at the two ends of a thermal link G_i. To a good approximation, every energy carrier departing at one end arrives instantly at the other end. This gives rise to a cross-spectral density term,

$$SC_i = -4k_B {T_i}^2 G_i \gamma. \tag{4.11}$$

The thermal fluctuations ST_{N+1} cause fluctuations of the current through

the voltage-biased thermistor. The spectral density is

$$SI_{thermal} = ST_{N+1} \times V_b^2 (dR/dT)^2 / R^4. \tag{4.12}$$

In addition there are two other independent sources of current noise in the system. Johnson noise from the bolometer and the bias resistor is suppressed by electrothermal feedback for $\omega \leq 1/\tau_0$ [20], while SQUID amplifier noise has a white spectrum. In the measurements described here, both are negligible.

Figure 4.1 shows a comparison between the model for $N = 20$ and noise spectra measured from devices 1, 2, and 3. We find good agreement for all three devices, which differ considerably in the heat capacities of thermistor and leads. The model also appears to adequately represent the effect of the added heat capacity in device 3. The results of our calculations do not change significantly if the parameter N is increased beyond 20. As discussed earlier, even the case $N = 1$ (two or three heat capacity models) yields a peak qualitatively similar to those observed.

We can use this model to predict how a change in design parameters will affect the bolometer noise. We find that it is possible to shift the noise peak to higher frequencies by selecting materials with lower heat capacity for the leads and absorber. In the present devices this can be done by making the leads from thin Nb film. To include the distributed heat capacity of

an optical absorber, we have extended the model by adding lumped heat capacities $C_{N+2}, C_{N+3}, \ldots$ connected to C_{N+1}. We have modeled absorber-coupled bolometers with low heat capacity components such as Nb leads and an Au absorber. We predict that, if excess heat capacities can be eliminated, such bolometers will achieve simple thermal fluctuation limited noise up to their maximum response frequency [2].

4.4 Conclusions

We have developed a model to explain the excess noise occurring in suspended voltage-biased superconducting bolometers. The model is supported by data from three devices designed specifically to test the theory. These devices show white noise at the fundamental limit set by thermal fluctuations at low frequencies (200mHz to 10-50Hz) and a wide peak of excess noise at higher frequencies. While this noise performance would already be adequate for many observations, our model predicts that the onset of excess noise can be shifted to much higher frequencies by reducing the heat capacities of bolometer components.

We thank J. Skidmore for his support.

Chapter 5

A VSB for Operation at 4K

In the laboratory, spectroscopy with Fourier transform spectrometers is the most important application for far-IR detectors. Currently, detectors used for this purpose are typically 4K composite bolometers [12] with semiconducting sensors and JFET amplifiers. Composite bolometers tend to have large heat capacity. To achieve a sufficiently fast response they are often designed with high values of G resulting in poor noise performance. As discussed in Section 1.1, Fourier spectroscopy benefits greatly from fast and highly linear detectors, making the VSB an ideal candidate to replace the existing technology. In this chapter we discuss the design, fabrication, and testing of a prototype for a VSB for this purpose. The test device consists of

a sensor and leads patterned on a LSN membrane. We discuss the addition of an absorber which is necessary to form a complete bolometer.

To design a bolometer for use for laboratory spectroscopy we first have to decide on values for the base temperature T_0 and for the average thermal conductance $\bar{G}$. In this case, the choice of T_0 is driven by practical constraints rather than by a required noise level for the detector as discussed in Section 3.1.1. To be accepted by the lab user community, the cryogenic technology has to be simple and convenient. We therefore decided to design a detector for $T_0 = 4.2$K which can be reached with liquid ^{4}He without pumping. This temperature range is now also easily accessible to mechanical cryo-coolers such as pulse-tube coolers.

To estimate the expected optical power on the bolometer we assume that the arc lamp used as a far-IR source in the spectrometer can be modeled as a black body with temperature T_{bb}. If the incoming signal passes through a low-pass filter with sharp cut-off at frequency ω_{max} the power absorbed in the bolometer is

$$P_{opt} = \epsilon A \frac{d\Omega}{4\pi} \frac{k_B T_{bb}}{3\pi^2 c^2} \omega_{max}^3, \tag{5.1}$$

where ϵ is the overall optical efficiency, A is the area of the absorber, $d\Omega$ is the solid angle from which the bolometer is illuminated, and $A \cdot d\Omega$ is

the throughput. For a filter which is transparent to wavelengths $\geq 200\mu$m, $\omega_{max} = 9.4$THz. For $T_{bb} = 1300$K, $A = 7\text{mm}^2$, and $\epsilon = 0.25$ we get $P_{opt} \approx 8 \cdot 10^{-7}$W. Assuming that $T_c - T_0 \approx 4$K, Equation 3.3 gives $\bar{G} \approx 10^{-6}$W/K. We find that a value of this order can be achieved using an unpatterned LSN membrane, considerably simplifying fabrication. For the design shown in Figure 5.1 we expect $\bar{G} \approx 1.6 \cdot 10^{-6}$W/K. (For a device without an absorber we expect a slightly lower value.) The value can be reduced by using a thinner LSN film and a larger membrane. The leads make a negligible contribution to $\bar{G}$.

Since P_{opt} depends on ω_{max}^3, the optimal value of $\bar{G}$ is strongly dependent on the filter used. However, it is possible to use the device described here for spectroscopy at shorter wavelengths by reducing the throughput of the spectrometer. For example, if a filter with $\omega_{max} = 94$THz is used,[1] the throughput has to be reduced by a factor 10^3.

For the sensor we require a material with $T_c > T_0$. Several pure metals exhibit transitions above 4.2K (Nb at 9.2K, Pb at 7.2K, La at 6.0K (fcc phase), V at 5.4K, and Ta at 4.5K). We chose to fabricate the sensor as well

[1] This corresponds to $\lambda \geq 20\mu$m which lies in the range accessible to commercial HgCdTe photovoltaic detectors operated at 77K.

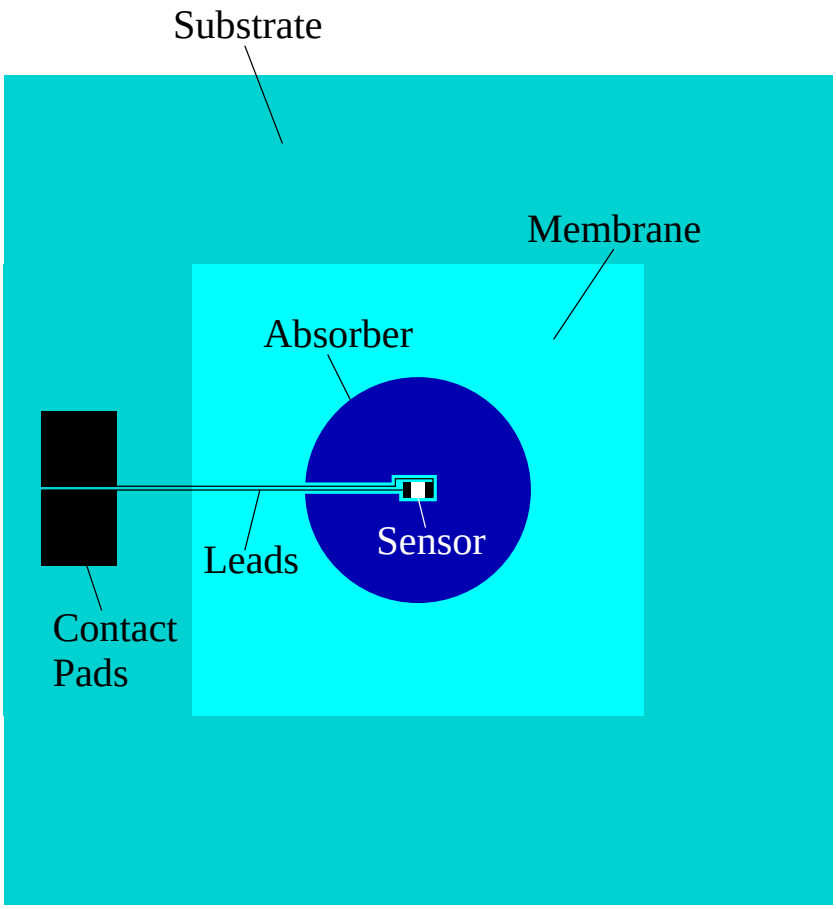

Figure 5.1: A drawing of the 4K VSB. A free standing 6mm×6mm LSN membrane holds 5μm wide leads making contact to a 95μm×95μm sensor in the center of a 3mm diameter absorber. In the drawing leads and sensor have been exaggerated in size.

as the leads out of Nb because it is widely used for lithographed devices and circuits. This makes it necessary to modify the transition temperature of either leads or sensor, since the leads have to be completely superconducting when the sensor is biased in its transition as discussed in Section 3.1.2. As the transition temperature of Nb is somewhat higher than optimal for $T_0 = 4.2\text{K}$, lowering the T_c of the sensor is favorable.

In a first approach we fabricated leads and sensor out of a thin film of Nb. A patch of Au was patterned underneath the sensor in order to reduce T_c by proximity effect [17]. This approach failed because the T_c of the Nb film did not shift. After being patterned in a lift-off procedure, the Au film was presumably not clean enough to make intimate contact with the Nb film. In addition, the Nb showed poor step coverage at the edge of the underlying Au patch, resulting in excess resistance.

Our current approach is based on the fact that for Nb films thinner than 1000Å the transition temperature depends on the film thickness as shown in Figure 5.2. By fabricating the sensor out of a 160Å thick Nb film, we can reduce T_c considerably from the bulk value.

The fabrication process relies only on standard microfabrication techniques. All features are defined using a 10:1 reduction wafer stepper and

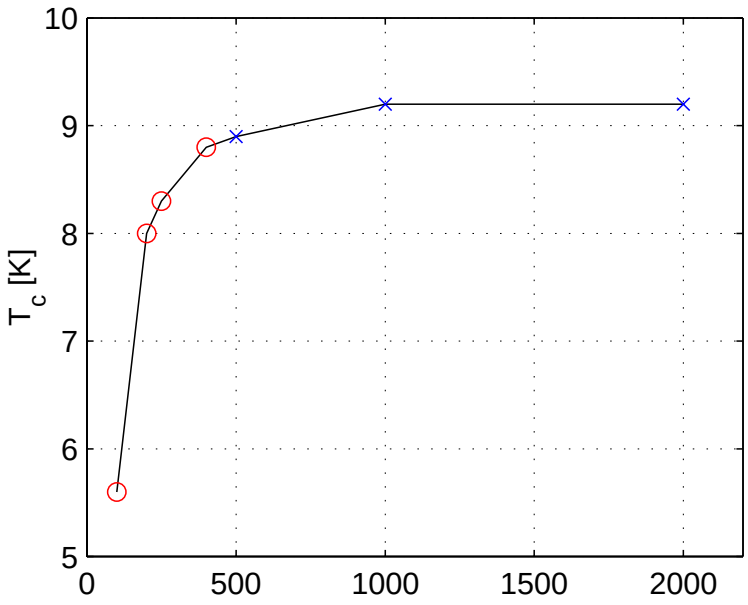

Figure 5.2: The T_c of Nb films as a function of film thickness. The data points marked with (x) are courtesy of X. Meng.

a standard photolithographic process. At first, a 1μm thick layer of LSN is deposited on the front and back of a standard Si wafer by Low Pressure Chemical Vapor Deposition (LPCVD). A 1000Å thick layer of Nb is deposited on the front of the wafer in a dedicated sputter deposition system with a base pressure of 8×10^{-8}torr. The Nb is removed from the area which will later hold the sensor with a fluorine-based plasma etch. A second, 160Å thick layer of Nb is deposited with the same deposition system. The sensor, leads, and contact pads are defined with photoresist and etched into the Nb with the same plasma etch. In this way leads and contact pads are made out of both Nb layers while the sensor only contains the second, thinner layer. We do not observe a contact resistance between the two layers even though they are deposited in separate vacuum steps. From the backside of the wafer a square window is etched into the LSN behind the bolometer. After dicing the wafer individual dyes are mounted in an etch jig which protects the front of the dye with a silicone rubber seal [36]. Using the LSN window frame on the backside as a mask, the Si substrate is etched away with an aqueous solution of KOH at 70°C. At the end of the etch only the free standing LSN membrane remains with leads and sensor on the front. Contact to the detector can be made with Al wire bonds. While these bonds are not superconducting at T_0,

their resistance is small enough to be tolerable. If necessary, contact could also be made with superconducting Nb wire bonds.

The bolometer was tested in a dark enclosure which was cooled to 4.2K with liquid ^{4}He. Figure 5.3 shows that the Nb sensor has a normal resistance of $R_N \approx 5\Omega$ and a resistive transition at $T_c = 8.13$K with the maximum transition steepness $\alpha = d\log R/d\log T$ of 8000. The maximum value of the loop gain, which is a measure of the strength of the feedback, was estimated to be $\mathcal{L} \approx 4000$.

Voltage bias was achieved by current biasing a 300mΩ shunt resistor. An unwanted resistance of 50mΩ in series with the device was accounted for in the data analysis. The bolometer current was measured with a commercial SQUID ammeter [24]. Noise spectra were computed with a spectrum analyzer [29]. An attenuated cold light-emitting diode [25] with λ =626nm was used as an optical stimulator. The power emitted by the diode was stepped up abruptly and the resulting change in the bolometer output was fitted to an exponential to determine the bolometer time constant.

We initially connected the SQUID input coil directly in series with the bolometer (cf. Figure 3.3), as was done for all low-T_c devices described earlier. However, when the bolometer was biased in the transition, the SQUID system

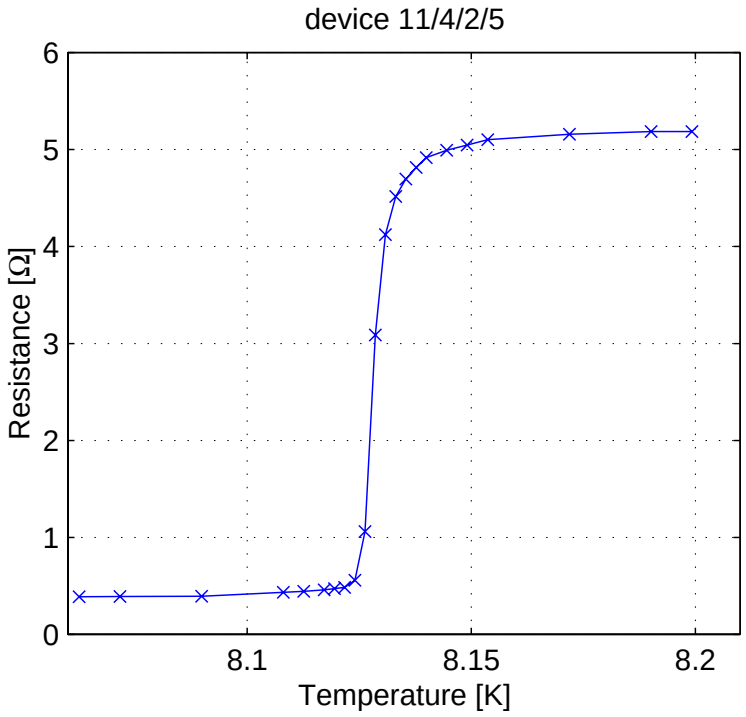

Figure 5.3: The resistive superconducting transition of a sensor made of a 160Å thick film of Nb. Low in the transition ($\approx 1\Omega$) $\alpha \approx 8000$.

lost lock, most likely because the noise level at high frequencies exceeded the available slew rate. To solve this problem we reduced the coupling to the SQUID by introducing an intermediate signal transformer, as is shown in Figure 5.4.

The secondary loop formed by the secondary coil of the transformer L_2 and the input coil of the SQUID L_3 has to be completely superconducting. Otherwise a DC signal in the bolometer circuit would result in a decaying signal in the SQUID output. When we initially used solder (a type-II superconductor) for L_2, frequent jumps were observed in the SQUID output, most likely due to flux quanta randomly entering and leaving the secondary loop. In a first design the coils L_1 and L_2 were wound on a normal conducting core resulting in high level excess white noise caused by Nyquist noise in the core. Our current transformer uses a primary made of NbTi wire, no transformer core, and a secondary made of Nb wire which makes superconducting contact to the SQUID input coil. The transformer reduces the signal by a factor

$$\zeta \cdot \frac{\sqrt{L_1 L_2}}{L_2 + L_3}, \tag{5.2}$$

where the coupling factor ζ for our design is $\approx 1/2$ [37].

The average thermal conductance of the bolometer was found to be $\bar{G} = 1.4 \cdot 10^{-6}$W/K in excellent agreement with prediction. Figure 5.5 shows

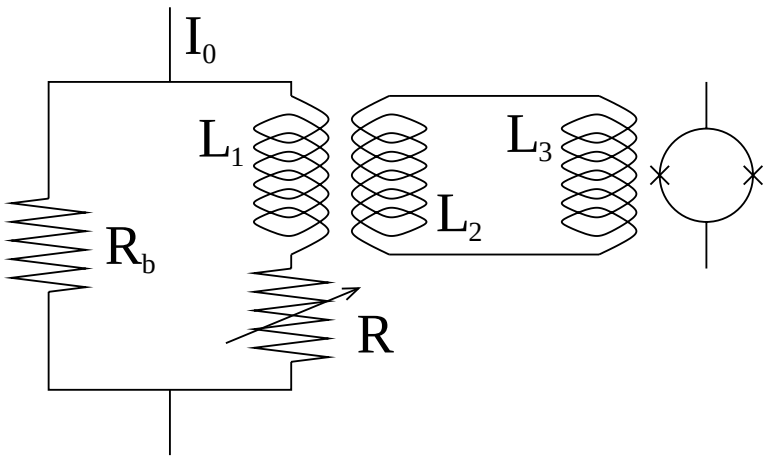

Figure 5.4: Bias circuit used for the 4K bolometer. The transformer consisting of L_1 and L_2 reduces the coupling to the SQUID. To preserve DC response, the secondary loop formed by L_2 and the SQUID input coil L_3 has to be completely superconducting.

the current noise spectral density for two different bias points. The observed noise level agrees well with theory. The rise in noise observed at low frequencies may be due to bubbles in the He bath. The onset at $\approx$ 10Hz is low enough for use in many continuously scanned interferometers which operate at fringe frequencies above 60Hz to avoid a 60Hz spike in the spectrum. A passive thermal filter could be used to reduce this source of low frequency noise. The rise at high frequencies is caused by a resonance in the SQUID system and is not intrinsic to the device.

Figure 5.6 shows an optical time constant measurement. The data cannot be fit well with a single exponential indicating that several different time constants are present. Directly after the change in LED power, the device responds with a time constant of $\approx$ 1ms. At a later time the data are best fit with a time constant of $\approx$ 6ms. We attribute this to the fact that the sensor is in more intimate thermal contact to the leads and to the center of the membrane than to other parts of the membrane, giving rise to a range of time constants. When a step is introduced in the bias voltage rather than in the optical power, yet a shorter time constant of $\approx 250\mu$s is observed. This effect is attributed to the internal thermalization process in the sensor and has also been observed in low-T_c VSBs.

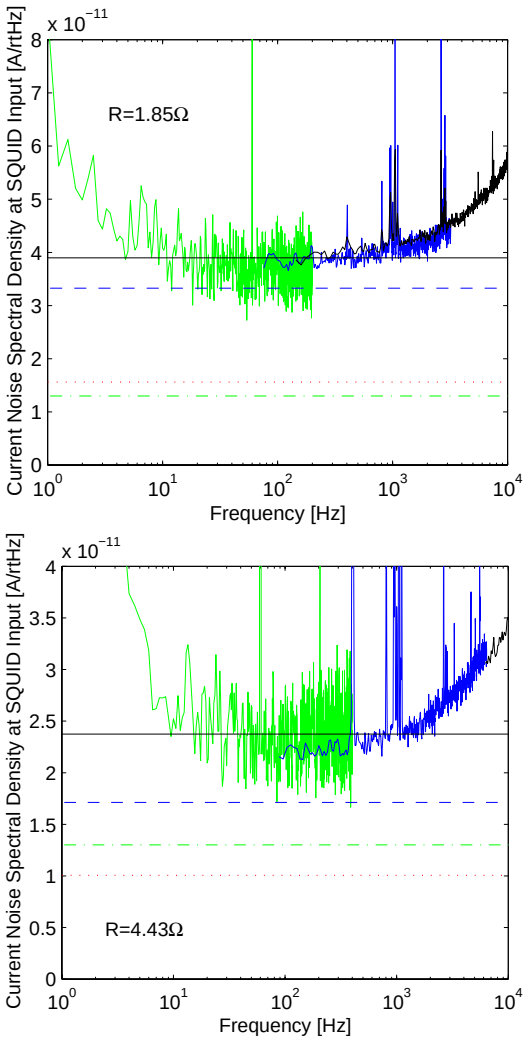

Figure 5.5: The upper/lower plot shows the current noise spectral density when the device is biased at a resistance of 1.85Ω/4.43Ω. The predicted level of the total noise (solid line) is the quadrature sum of thermal fluctuation noise (dashed line), SQUID noise (dash-dot), and Johnson noise (dotted).

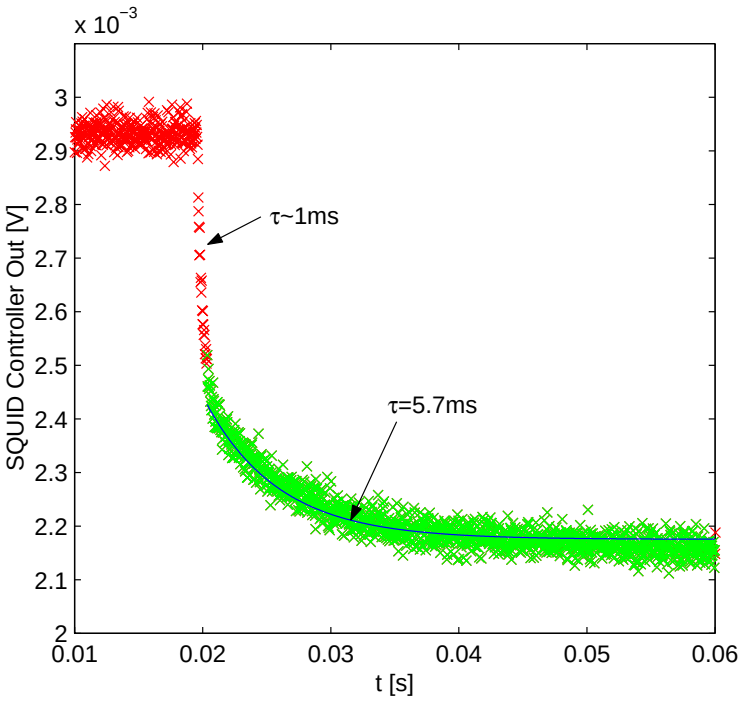

Figure 5.6: Time constant data measured by abruptly changing the optical power does not fit a single exponential. A range of time constants from $<$ 1ms to $>$ 6ms appears to be present.

To complete the bolometer, an absorber must be added to the present device. By choosing a material with high resistivity, such as Bi, we can deposit the absorber directly with the right resistance per square. A Bi film with the correct resistance of $377\Omega/\square$[2] is 31Å thick. Films of highly conducting metals such as Au cannot be made thin enough to have the right resistance[3] and therefore would have to be patterned lithographically. The absorber can be fabricated in either of two ways:

- After the membrane has been released, it can be evaporated onto the backside of the membrane through a shadow mask which protrudes into the cavity in the Si substrate.

- Before the wafer is diced, it can be deposited on the front of the device and patterned by a simple lift-off procedure. By using the shape depicted in Figure 5.1, shorting the sensor or leads electrically can be avoided.

The absorber will make a negligible contribution to the total heat capacity and to the thermal conductance within the absorber area. We therefore

[2] see Appendix A

[3] A Au film with the correct resistance of $377\Omega/\square$ would have to be only 0.6Å thick. This thickness cannot be achieved with standard deposition methods.

expect the complete bolometer to show the same time constants as the device discussed here.[4]

To maximize absorption a reflector can be placed at a distance of $\lambda/4$ behind the bolometer in a fashion similar to Figure 3.11.

We thank J. Clarke and X. Meng for helpful discussions and J. Skidmore for his contributions in testing the device and in building the test setup. We are indebted to X. Meng for providing us with high quality Nb films.

[4]The measurements discussed here rely on the fact that some of the visible light emitted by the diode is absorbed in the LSN membrane. The optical power is therefore deposited uniformly over the whole membrane. In a complete device, the incoming far-IR waves are predominantly absorbed in the absorber. This is expected to shorten the observed time constant slightly.

Appendix A

Optical Coupling in the Presence of a Si Substrate

Here we discuss the absorption of an optical signal in a bolometer with a reflector deposited on the backside of the Si substrate, as discussed in Section 3.3. We consider the idealized case of Figure A.1, not taking into account effects at the edges of the bolometer: The signal beam propagates through vacuum and is incident on the absorber mesh characterized by a sheet resistance $R_{\square}$. Behind the mesh there is a vacuum gap of width a, a dielectric with index of refraction n' of thickness b/n', and a perfect reflector. For silicon $n' \approx \sqrt{12}$. We set the incident amplitude to unity. The

transmitted amplitude at the absorber mesh is t, the reflected amplitude is r. (The transmissivity, reflectivity, and absorptivity are $T = t^2$, $R = r^2$, and $A = 1 - T - R$, respectively.) The interface between the vacuum and the dielectric differs from that at the absorber in two respects:

- There is no absorption. $A' = 1 - R' - T' = 0$
- The problem is not symmetric with respect to the plane of the interface. Therefore, we have to distinguish between the reflection amplitude for a beam incident from the left r'_l and that for a beam from the right r'_r. In general, $r'_l \neq r'_r$ and by the same token $t'_l \neq t'_r$.

To understand absorption and reflection in this system, it is instructive to first consider the hypothetical case where $r'_l = 1$ and $t'_l = 0$, i.e. where the dielectric is replaced by a perfect reflector. In this case the reflected wave is composed of a component reflected by the absorber directly and of components which have been reflected by the dielectric and the absorber $1, 3, 5, \ldots$ times. The total reflected amplitude is

$$\begin{aligned} \rho &= r + \\ &\quad t^2 e^{2ika} r'_l \times \left[1 + \left(r r'_l e^{2ika}\right) + \left(r r'_l e^{2ika}\right)^2 + \left(r r'_l e^{2ika}\right)^3 + \ldots\right] \\ &= r + \frac{r'_l t^2}{e^{-2ika} - r r'_l}, \end{aligned} \tag{A.1}$$

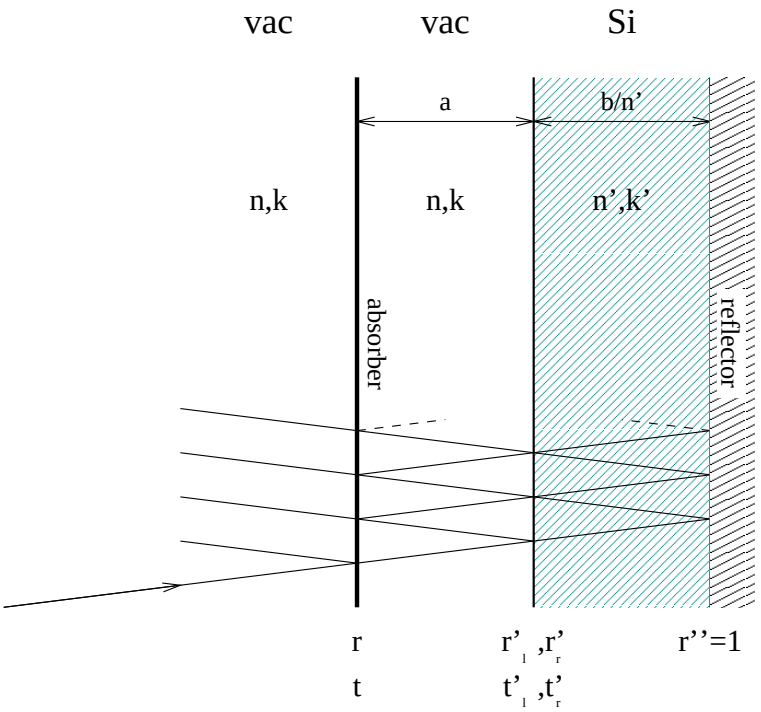

Figure A.1: Cross-section of an absorber suspended over a Si substrate and a reflector. The optical signal is incident from the left and is partially reflected in the plane of the absorber and at the interface between vacuum and Si. All transmitted light is reflected by a superconducting reflector at the far right. For better illustration the beams are drawn at an angle to the surface, even though we consider only the case of normal incidence.

where $k = 2\pi/\lambda$ is the wave number of the signal in vacuum. By applying boundary conditions at the plane of the absorber one finds

$$r = \frac{Z_0/R_\square}{2 + Z_0/R_\square} \qquad t = \frac{2}{2 + Z_0/R_\square}, \tag{A.2}$$

where $Z_0 = 377\Omega$ is the impedance of free space and $R_\square$ is the square resistance of the absorber. If we choose $a = \lambda/4$ and $R_\square = Z_0$, then $r = 1/3$ and $t = 2/3$ and we get $\rho = 0$. This is the well known result that perfect absorption is achieved when the absorber is matched to Z_0 and a reflector is placed a distance $\lambda/4$ behind the absorber in vacuum.

To include the layer of dielectric in the calculation, i.e. to consider the case where $r_l' < 1$, we have to replace r_l' in equation A.1 with the *total* reflected amplitude ρ' of the dielectric layer,

$$\rho = r + \frac{\rho' t^2}{e^{-2ika} - r\rho'}. \tag{A.3}$$

Here, ρ' is the reflected amplitude for a beam of unity amplitude incident on the dielectric. Analogous to equation A.1 we get

$$\begin{aligned} \rho' &= r_l' + t_l t_r e^{2ikb} r'' \times \left[1 + \left(r_r' r'' e^{2ikb}\right) + \left(r_r' r'' e^{2ikb}\right)^2 + ...\right] \\ &= r_l' + \frac{r'' t_l t_r}{e^{-2ikb} - r_r' r''}. \end{aligned} \tag{A.4}$$

Note that $\mid \rho' \mid = 1$ always, as should be the case since no power is dissipated in the dielectric or the reflector. This means that by replacing r'_l with ρ' in equation (A.1) we merely introduce an additional phase factor.

The transmission and reflection amplitudes at the interface between vacuum and dielectric are determined by the refractive indices of the two media[1][38]:

$$r'_l = \frac{n - n'}{n + n'} \tag{A.5}$$

$$t'_l = \frac{2n}{n + n'} \tag{A.6}$$

$$r'_r = \frac{n' - n}{n + n'} \tag{A.7}$$

$$t'_r = \frac{2n'}{n + n'}. \tag{A.8}$$

We see that $r'_l < 0$, which means that the phase is inverted upon reflection from the dielectric.

Figure A.2 shows a plot of $1 - \rho$ as a function of ka and of $kb = k' \times b/n'$. In areas where $1 - \rho = 1$, the reflected amplitude is zero and all energy is absorbed. This is the case one would ideally like to achieve for a detector. As is to be expected, this case is achieved for $a = \lambda/4$, $b = 0$ and for $a = 0$,

[1] At the interface between vacuum and dielectric the reflectivity for light incident from the left is $R' = r'^2_l$ and the transmissivity is $T' = t'^2_l \times n'/n$. Therefore $R' + T' = 1, \quad A' = 0$.

$b = \lambda/4$. There is also a continuous curve connecting these two points on which the condition $1 - \rho = 1$ is met (the ridge in the 3-dimensional plot). This means that for every $a < \lambda/4$ one can find a b (and vice versa) so that absorption is, at least in the idealized model, perfect.

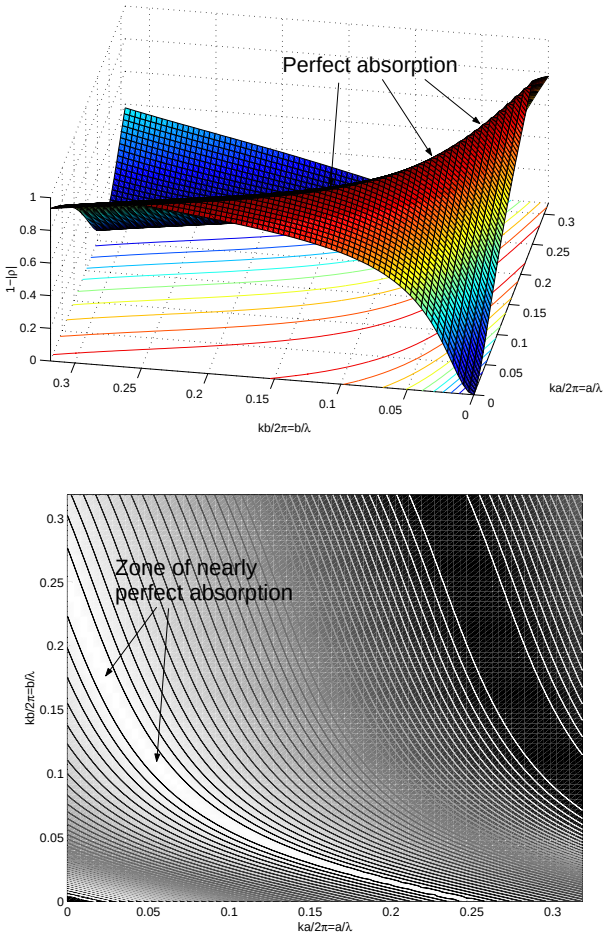

Figure A.2: Top: A 3-dimensional plot of $1 - \rho$ as a function of ka and of $kb = k' \times b/n'$. Bottom: A contour plot of the same function.

Appendix B

Accounting for a Non-Ideal Voltage-Bias

Voltage-bias is achieved in all our devices by current-biasing a small resistor R_b in parallel to the detector and SQUID input coil (see Figure 3.3). To achieve a perfect voltage-bias, the bias-resistance R_b would have to be infinitely small. In reality, R_b is a finite fraction of the bolometer resistance R, and an excess resistance R_{xs} in series with R is typically observed (see Figure B.1), which moves the system away from an ideal voltage-bias. Here we summarize the combined effects of finite R_b and R_{xs} on the important operational parameters of the bolometer.

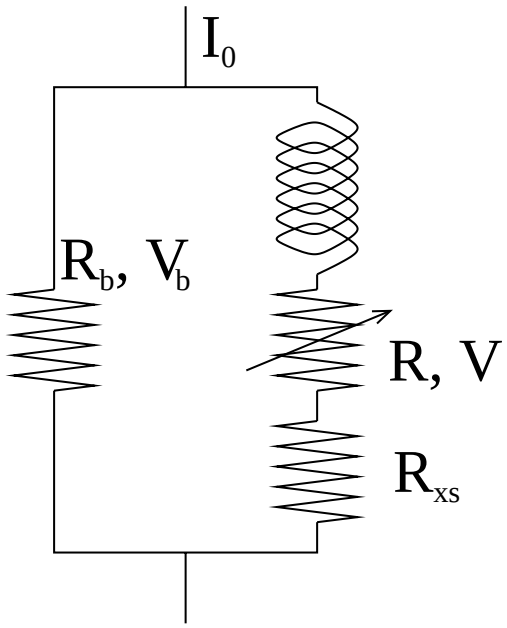

Figure B.1: The bias circuit used for all devices reported in this thesis. A small bias resistor R_b is put in parallel with the SQUID input coil and the bolometer R. Some excess resistance R_{xs} in series with the bolometer is usually observed. By current-biasing this circuit the bolometer is effectively voltage-biased as long as $R_b + R_{xs} \ll R$.

Our results take a simple form if we express them in terms of the parameter

$$\eta = \frac{R_b + R_{xs}}{R}. \tag{B.1}$$

Let I_0 be the constant bias current through the circuit as a whole, V the voltage seen by R, and V_b the voltage seen by R_b. Then

$$V_b = \frac{I_0}{\frac{1}{R_b} + \frac{1}{R+R_{xs}}} = \frac{I_0}{1 + \frac{R_b}{R+R_{xs}}}, \tag{B.2}$$

and

$$V = V_b \cdot \frac{R}{R + R_{xs}} = \frac{I_0 R_b}{1+\eta}. \tag{B.3}$$

We find

$$\frac{dP_b}{dR} = -\frac{V^2}{R^2}\frac{1-\eta}{1+\eta}. \tag{B.4}$$

The effective thermal conductance defined in equation 2.10 becomes

$$G_{eff} = \frac{P_b \alpha}{T_t}\frac{1-\eta}{1+\eta} + G + i\omega C, \tag{B.5}$$

and therefore the loop gain is

$$\mathcal{L}(\omega) = -\frac{dP_b}{dP_{tot}} = \frac{\mathcal{L}}{1+i\omega\tau_0}, \quad \text{with} \quad \mathcal{L} = \frac{P_b\alpha}{GT_t}\left(\frac{1-\eta}{1+\eta}\right). \tag{B.6}$$

The current responsivity (cf. equation 2.13) is

$$S_I = \frac{dI}{dP_{opt}} = \frac{dI}{dP_b} \cdot \frac{dP_b}{dP_{opt}} = \frac{1}{V} \cdot \frac{1}{1-\eta} \cdot \frac{dP_b}{dP_{opt}} \tag{B.7}$$

$$= \frac{1}{I_0 R_b} \cdot \frac{1+\eta}{1-\eta} \cdot \frac{dP_b}{dP_{opt}} \tag{B.8}$$

$$= -\frac{1}{I_0 R_b} \cdot \frac{1+\eta}{1-\eta} \cdot \frac{\mathcal{L}}{\mathcal{L}+1} \cdot \frac{1}{1+i\omega\tau}. \tag{B.9}$$

Note that η depends on R. In contrast to Equation 2.13 the responsivity is therefore not completely immune to changes in the base temperature T_0 and the optical loading anymore. For this reason η should always be kept to a minimum.

Even though the magnitude of S_I is increased, that of dI/dT_t is reduced:

$$\frac{dI}{dR} = -\frac{V}{R^2}\frac{1}{1+\eta}, \tag{B.10}$$

so

$$\frac{dI}{dT_t} = -\frac{V}{R^2}\frac{dR}{dT_t}\underbrace{\frac{1}{1+\eta}}_{(*)}. \tag{B.11}$$

This means that for a given spectral density of temperature fluctuations the resulting spectral density of current fluctuations is actually reduced by the square of the factor (*) at all frequencies (cf. equation 4.12):

$$SD_I(\omega) = \underbrace{\frac{V^2}{R^4}\left(\frac{dR}{dT_t}\right)^2 \cdot \frac{1}{(1+\eta)^2}}_{(dI/dT_t)^2} \cdot \frac{\tau^2}{\tau_0^2} \cdot \frac{1+\omega^2\tau_0^2}{1+\omega^2\tau^2} SD_{T_t}(\omega). \tag{B.12}$$

Appendix C

A Model with Two Heat Capacities

In chapter 4 we developed a model for the thermal response of a system of $N + 1$ heat capacities connected by thermal links. Our calculations can be understood more easily if one first considers the much simpler case of only two heat capacities. This model is derived here. While it does predict a peak in the noise spectrum, the quantitative agreement with data from our devices is poor.

Figure C.1 shows the simple thermal model used here. A heat capacity C_1 is connected to a thermal bath of temperature T_0 by a thermal conductance

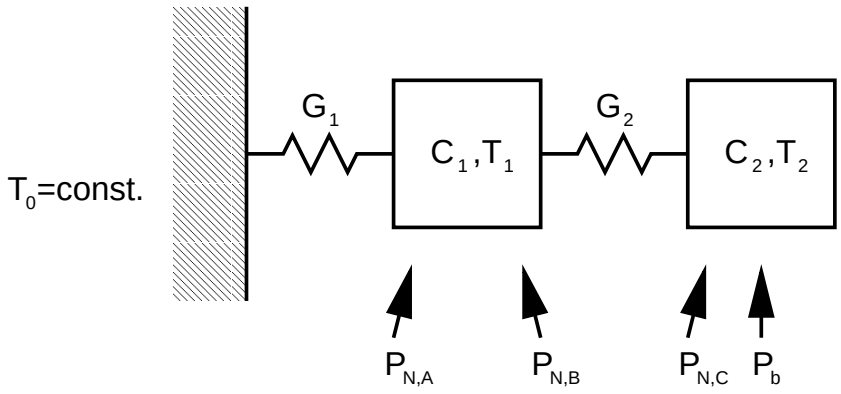

Figure C.1: A heat capacity C_1 is connected to a thermal bath of temperature T_0 by a thermal conductance G_1. A second heat capacity C_2 is connected to C_1 by a thermal conductance G_2. The sensor is part of C_2.

G_1. A second heat capacity C_2 is connected to C_1 by a thermal conductance G_2. Here we consider the case where the sensor is part of C_2 and hence the bias power P_b is absorbed in C_2.[1] Thermal fluctuation noise arising in G_1 is seen by C_1 as the noise power $P_{N,A}$. Thermal fluctuation noise arising in G_2 is seen by C_1 and C_2 as the noise power $P_{N,B}$ and $P_{N,C}$, respectively.

Any change in noise power or bias power will result in a change of the temperatures T_1 and T_2. This response depends on the frequency of the excitation because a heat capacity connected to a thermal conductance effectively acts as a low-pass filter for thermal changes. The following matrix equation describes the model system,

$$\begin{pmatrix} \delta P_{N,A} + \delta P_{N,B} \\ \delta P_{N,C} + \delta P_b \end{pmatrix} e^{i\omega t} =$$

$$\underbrace{\begin{pmatrix} i\omega C_1 + G_1 + G_2 & -G_2 \\ -G_2 & i\omega C_2 + G_2 \end{pmatrix}}_{(*)} \times \begin{pmatrix} \delta T_1 \\ \delta T_2 \end{pmatrix} e^{i\omega t}, \tag{C.1}$$

where (*) is the equivalent of matrix M in equation 4.4. When the sensor is

[1] The case where P_b is absorbed in C_1 can be treated in the same fashion and yields qualitatively similar results.

biased with a voltage V_b at resistance R, then

$$P_b = \frac{{V_b}^2}{R} \quad \Longrightarrow \quad \frac{dP_b}{dT_2} = -\frac{{V_b}^2}{R^2}\frac{dR}{dT_2}, \tag{C.2}$$

so that

$$\delta P_b = -\frac{P_b \alpha}{T_2}\delta T_2, \tag{C.3}$$

with $\alpha = d\log R/d\log T$, as usual.

Including the feedback and omitting the time dependence, equation C.1 becomes

$$\begin{pmatrix} \delta P_{N,A} + \delta P_{N,B} \\ \\ \delta P_{N,C} \end{pmatrix} =$$

$$\begin{pmatrix} i\omega C_1 + G_1 + G_2 & -G_2 \\ \\ -G_2 & i\omega C_2 + G_2 + \frac{P_b \alpha}{T_2} \end{pmatrix} \cdot \begin{pmatrix} \delta T_1 \\ \\ \delta T_2 \end{pmatrix}. \tag{C.4}$$

The inverse equations are

$$\begin{pmatrix} \delta T_1 \\ \\ \delta T_2 \end{pmatrix} = \frac{1}{\det} \begin{pmatrix} i\omega C_2 + G_2 + \frac{P_b \alpha}{T_2} & G_2 \\ \\ G_2 & i\omega C_1 + G_1 + G_2 \end{pmatrix}$$

$$\cdot \begin{pmatrix} \delta P_{N,A} + \delta P_{N,B} \\ \\ \delta P_{N,C} \end{pmatrix}, \tag{C.5}$$

where

$$\det = \left(i\omega C_2 + G_2 + \frac{P_b \alpha}{T_2}\right) \cdot (i\omega C_1 + G_1 + G_2) - {G_2}^2. \tag{C.6}$$

Ultimately, we are interested in the fluctuations of the current, i.e. of the bolometer signal, which result from the thermal fluctuation noise in G_1 and G_2. For a given bias voltage, the current through the bolometer is entirely determined by R which in turn is a function only of T_2. From the second line of equation (C.5) we can write the spectral density of the fluctuations of T_2. To a good approximation any energy carrier entering G_2 at one end appears instantly at the other. Therefore $\delta P_{N,B}$ and $\delta P_{N,C}$ are correlated. Assuming that $\delta P_{N,A}$ is not correlated with the other terms we get:[2]

$$S_{T_2}(\omega) = \left(\frac{1}{\mid \det \mid}\right)^2 \cdot \Big[{G_2}^2 \cdot (S_{N,A}(\omega) + S_{N,B}(\omega))$$

$$+ \mid i\omega C_1 + G_1 + G_2 \mid^2 \cdot S_{N,C}(\omega)$$

$$+2 \cdot \mid i\omega C_1 G_2 + G_1 G_2 + {G_2}^2 \mid \cdot S_{N,B,C}(\omega)\Big], \qquad \text{(C.7)}$$

[2] If $X(t)$ is the input to a linear system with transfer function $g(f)$ and $Y(t)$ is the output of the system, then $\widetilde{Y(t)} = g(f) \cdot \widetilde{X(t)}$ (and by the convolution theorem $Y(t) = \widetilde{g(f)} * X(t)$). Since we assume the system to be linear, for two drivers we get $Y(t) = \widetilde{g_1(f)} * X_1(t) + \widetilde{g_2(f)} * X_2(t)$. By the convolution theorem: $\widetilde{Y(t)} = g_1(f) \cdot \widetilde{X_1(t)} + g_2(f) \cdot \widetilde{X_2(t)}$. The spectral intensity of $Y(t)$ then is:

$$S_y(f) = S_{x1}(f) \cdot \mid g_1(f) \mid^2 + S_{x2}(f) \cdot \mid g_2(f) \mid^2 + 2 \cdot S_{corr}(f) \cdot \mid g_1(f) \mid \cdot \mid g_2(f) \mid .$$

where $S_{N,A}(\omega)$, $S_{N,B}(\omega)$, and $S_{N,C}(\omega)$ are the noise spectral densities corresponding to $P_{N,A}$, $P_{N,B}$, and $P_{N,C}$ respectively. Here $S_{N,B,C}(\omega)$ is the cross-spectral density due to correlations. This is the equivalent of equation 4.9.

Bibliography

[1] J.M. Gildemeister, Adrian T. Lee, and P.L. Richards, A fully lithographed voltage-biased superconducting spiderweb bolometer, Appl. Phys. Lett., vol. 74, no. 6, p. 868 (1999)

[2] J.M. Gildemeister, Adrian T. Lee, and P.L. Richards, Monolithic arrays of absorber-coupled voltage-biased superconducting bolometers, accepted for publication in Appl. Phys. Lett.

[3] J.M. Gildemeister, Adrian T. Lee, and P.L. Richards, A model for excess noise in voltage-biased superconducting bolometers, submitted to Applied Optics.

[4] A.A. Penzias and R.W. Wilson, Determination of the Microwave Spectrum of Galactic Radiation, Astrophysical Journal, **146**, 666 (1966)

[5] G.F. Smoot, C.L. Bennett, A. Kogut, J. Aymon, C. Backus, et al., ApJ **360**, 685 (1990)

[6] P. DeBernardis, et al., Nature **404**, 995 (2000)

[7] S. Hanany, et al., submitted to ApJ, astro-ph/0005123 (2000)

[8] J.A. Tauber, The current status of PLANCK, Proceedings of the XXXIIIth Moriond Conference, Les Arcs, France (1998)

[9] G.H. Rieke, Detection of light, Cambridge University Press, Cambridge, New York, Melbourne (1994)

[10] S.P. Langley, Nature **25**, 14 (1881?)

[11] E.E. Haller, Infrared Phys. **25**, 27 (1985)

[12] P.L. Richards, Bolometers for infrared and millimeter waves, J. Appl. Phys., vol. 76, no. 1, p. 1 (1994)

[13] J.C. Mather, Bolometer noise: nonequilibrium theory, Appl. Opt., vol. 21, no. 6, p. 1125 (1982)

[14] J.J. Bock, D. Chen, P.D. Mauskopf, and A.E. Lange, Space Science Reviews **74**, 229 (1995)

[15] C. Keller, Microfabricated high aspect ratio silicon flexures, MEMS Precision Instruments, El Cerrito (1998)

[16] P.B. Chu, J.T. Chen, R. Yeh, G. Lin,J.C.P. Huang, B.A. Warneke, S.J. Pister, Controlled pulse-etching with xenon difluoride, Proceedings of International Solid State Sensors and Actuators Conference (Transducers '97), Chicago, IEEE (1997)

[17] N.R. Werthamer, Theory of the superconducting transition termperature and energy gap function of superposed metal films, Phys. Rev., **132**, 2440 (1963)

[18] M. Myers, private communication

[19] Adrian T. Lee, P.L. Richards, Sae Woo Nam, Blas Cabrera, and K.D. Irwin, A superconducting bolometer with strong electrothermal feedback, Appl. Phys. Lett., vol. 69, no. 12, p. 1801 (1996)

[20] Shih-Fu Lee, J.M. Gildemeister, W.A. Holmes, Adrian T. Lee, and P.L. Richards, Voltage-biased superconducting transition-edge bolometer with strong electrothermal feedback operated at 370mK, Appl. Opt., vol. 37, no. 16, p. 3391 (1998)

[21] K.D. Irwin, An application of electrothermal feedback for high resolution cryogenic particle detection, Appl. Phys. Lett., vol. 66, no. 15, p. 1998 (1995)

[22] J.A. Chervenak, E.N. Grossman, K.D. Irwin, J.M. Martinis, C.D. Reintsema, C.A. Allen, D.I. Bergman, S.H. Moseley, and R. Shafer, Performance of multiplexed SQUID readout for cryogenic sensor arrays, Nucl. Inst. and Meth. A, vol. 444, no. 1-2 (2000)

[23] A.T. Lee, Shih-Fu Lee, J.M. Gildemeister, and P.L. Richards, Proceedings of the 7th International Workshop on Low Temperature Detectors LTD-7, Max Planck Institute of Physics, Munich, Germany (1997)

[24] Quantum Design, series 50 SQUID and model 550 controller

[25] Hewlett-Packard, model HLMP-1000

[26] J. Yoon, J. Clarke, J.M. Gildemeister, A.T. Lee, M. Myers, P.L. Richards, and J. Skidmore, A single SQUID multiplexer for arrays of low temperature sensors, submitted to Appl. Phys. Lett.

[27] D.J. Benford, E. Serabyn, T.G. Phillips, and S.H. Moseley, Proceedings of Advanced Technology MMW, Radio, and Terahertz Telescopes 1998, Kona, Hawaii, SPIE Vol. 3357 (1998)

[28] P. Agnese, C. Buzzi, P. Rey, L. Rodriguez, J.-L. Tissot, Proceedings of Infrared Technology and Applications XXV, Orlando, Florida, SPIE Vol. 3698 (1999)

[29] Stanford Research, model SR785

[30] J. Bock, J. Glenn, S. Grannan, K. Irwin, A. Lange, H. LeDuc, and A. Turner, Proceedings of Advanced Technology MMW, Radio, and Terahertz Telescopes 1998, Kona, Hawaii, SPIE Vol. 3357 (1998)

[31] J. Bhardwaj, H. Ashraf, and A. McQuarrie, Proceedings of the Third International Symposium on Microstructures and Microfabricated Systems, Montreal, Canada, Electrochem. Soc. (1997)

[32] K.D. Irwin, private communication.

[33] J.J. Bock, private communication.

[34] Electron Probe Microanalysis, Cameca SX-51 with high resolution wavelength dispersive spectrometers

[35] David Miller, Submillimeter residual losses in high-Tc superconductors, PhD thesis, UC Berkeley, 1993.

[36] Dow Corning, HS II RTV

[37] J. Yoon, personal communication

[38] J.D. Jackson, Classical Electrodynamics, John Wiley & Sons, New York, Chichester, Brisbane, Toronto, Singapore (1975)